

Probing the depths of the India-Asia collision: U-Th-Pb monazite chronology of granulites from NW Bhutan

C. J. Warren,¹ D. Grujic,² D. A. Kellett,^{2,3} J. Cottle,^{3,4} R. A. Jamieson,² and K. S. Ghalley⁵

Received 3 April 2010; revised 12 October 2010; accepted 24 November 2010; published 10 March 2011.

[1] Rocks metamorphosed to high temperatures and/or high pressures are rare across the Himalayan orogen, where peak metamorphic conditions recorded in the exposed metamorphic core, the Greater Himalayan Sequence (GHS), are generally at middle to upper amphibolite facies. However, mafic garnet-clinopyroxene assemblages exposed at the highest structural levels in Bhutan, eastern Himalaya, preserve patchy textural evidence for early eclogite-facies conditions, overprinted by granulite-facies conditions. Monazite hosted within the leucosome of neighboring granulite-facies orthopyroxene-bearing felsic gneiss yields LA-MC-ICP-MS U-Th-Pb ages of 13.9 ± 0.3 Ma. Monazite associated with sillimanite-grade metamorphism in granulite-hosting migmatitic gneisses yields U-Th-Pb rim ages between 15.4 ± 0.8 Ma and 13.4 ± 0.5 Ma. Monazite associated with sillimanite-grade metamorphism in gneiss at structurally lower levels yields U-Pb rim ages of 21–17 Ma. These data are consistent with Miocene exhumation of GHS material from a variety of crustal depths at different times along the Himalayan orogen. We propose that these granulitized eclogites represent lower crustal material exhumed by tectonic forcing over an incoming Indian crustal ramp and that they formed in a different tectonic regime to the ultrahigh-pressure eclogites in the western Himalaya. Their formation and exhumation in the Miocene therefore do not require diachroneity in the timing of the initial India-Asia collision.

Citation: Warren, C. J., D. Grujic, D. A. Kellett, J. Cottle, R. A. Jamieson, and K. S. Ghalley (2011), Probing the depths of the India-Asia collision: U-Th-Pb monazite chronology of granulites from NW Bhutan, *Tectonics*, 30, TC2004, doi:10.1029/2010TC002738.

1. Introduction

[2] The pressure-temperature-time (PTt) evolution of metamorphic rocks provides insight into a range of tectonic processes including crustal recycling, crustal and mantle geochemical evolution, and convergent plate boundary processes. PTt data also provide valuable constraints on the development, testing and refinement of large-scale geodynamic models. In the Himalayan orogen, considered to be the type locality for continental collision, metamorphic rocks recording high pressures (HP, >1.4 GPa) and/or high temperatures (HT, $>800^\circ\text{C}$) are rare, despite the extensively thickened crust (up to 70 km) and long-lasting convergence (since ~ 55 –50 Ma [Rowley, 1996, 1998; Zhu *et al.*, 2005]). The majority of the rocks that form the exposed high-grade core of the Himalayas (the Greater Himalayan Sequence or GHS), were metamorphosed at peak temperatures of $\sim 650^\circ\text{C}$ – 750°C during the Miocene, and experienced Barrovian-style regional metamorphism during the Eocene-Oligocene (see review in the work of Hedges [2000]).

[3] Contrasting occurrences of HP rocks have been described from the NW and E Himalaya but are yet to be reported from the central part of the orogen [Lombardo and Rolfo, 2000]. In the NW Himalayan regions of Kaghan and Tso Morari (Figure 1a), rocks immediately south of the India-Asia suture preserve evidence for Eocene ultrahigh-pressure (UHP) metamorphism to >2.7 GPa [de Sigoyer *et al.*, 2000; Kaneko *et al.*, 2003; Leech *et al.*, 2005; Parrish *et al.*, 2006; Epard and Steck, 2008]. These data suggest that the leading edge of the Indian continental margin was subducted, detached and exhumed to midcrustal levels within 10 Ma of the India-Asia collision at circa 55–50 Ma.

[4] In contrast, rare exposures of HP rocks in the E Himalaya are exposed in the metamorphic core of the orogen (hundreds of kilometers south of the India-Asia suture), and yield only cryptic evidence for >1.4 GPa HP metamorphism: the Ama Drime Range (Nepal/Tibet), Arun Valley (Nepal), Sikkim (India) and NW Bhutan (Figure 1a). In general, these rocks have been pervasively overprinted at post-peak-pressure high-temperature granulite-facies metamorphic conditions [Lombardo *et al.*, 1998; Liu *et al.*, 2005; Chakungal, 2006; Groppo *et al.*, 2007; Liu *et al.*, 2007; Rolfo *et al.*, 2008; Cottle *et al.*, 2009a; Chakungal *et al.*, 2010; Corrie *et al.*, 2010; Kali *et al.*, 2010]. It is as yet unclear whether these rocks formed in a subduction zone and therefore suggest diachronous India-Asia collision [Guillot *et al.*, 1999, 2008], whether they represent a deeper structural level of the GHS not exposed, preserved, or yet

¹Department of Earth and Environmental Sciences, CEPSAR, Open University, Milton Keynes, UK.

²Department of Earth Sciences, Dalhousie University, Halifax, Nova Scotia, Canada.

³Department of Earth Science, University of California, Santa Barbara, California, USA.

⁴NERC Isotope Geoscience Laboratories, British Geological Survey, Keyworth, UK.

⁵Geological Survey of Bhutan, Department of Geology and Mines, Ministry of Economic Affairs, Thimphu, Bhutan.

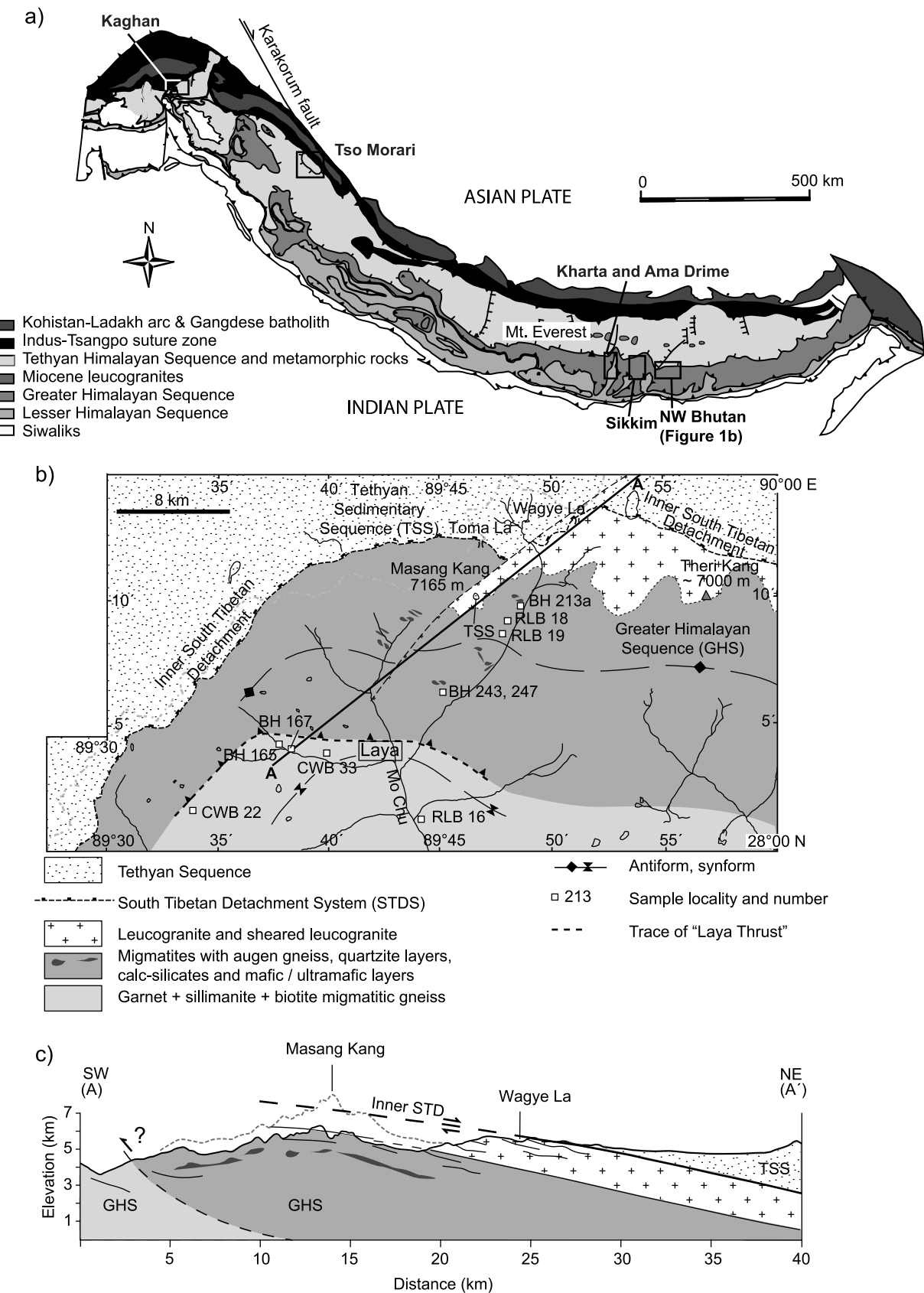


Figure 1

recognized elsewhere in the orogen, or whether they record an eastward change in collision or subduction regime.

[5] The thermobarometric conditions and timing of both HP metamorphism and the HT overprint in the E Himalaya remain unclear. Recent Lu-Hf analyses of garnets from putative eclogite-facies mafic rocks from the Arun Valley suggest that garnet grew at 20.7 ± 0.4 Ma [Corrie et al., 2010], which, if representative of garnet growth along the prograde path, indicates that eclogite-facies conditions were reached 20–25 Ma later than in the NW Himalaya. Monazite and xenotime U-Pb ages of granulitized eclogites in the Ama Drime Range (Nepal/Tibet) constrain granulite-facies metamorphism and associated anatexis to $<13.2 \pm 1.4$ Ma [Cottle et al., 2009a]. Monazites in migmatitic paragneisses and orthogneisses in the region yield similar ages from 13.4 ± 1.0 to 11.0 ± 3.3 Ma [Liu et al., 2007; Cottle et al., 2009a; Kali et al., 2010]. Following Kelsey et al. [2008], these ages are interpreted to represent monazite growth at the melt solidus during exhumation and cooling following the attainment of granulite facies conditions.

[6] Rocks of similar texture, petrology and mineral chemistry are exposed in NW Bhutan at the highest structural levels of the GHS. Here we present petrographic descriptions and laser ablation-multicollector-inductively coupled plasma-mass spectrometer (LA-MC-ICP-MS) U-(Th)-Pb monazite data from pelitic garnet-orthopyroxene granulites and their host garnet-biotite-sillimanite migmatitic gneisses. These rocks contain monazite, a potentially sensitive geochronometer that can be linked directly to bulk-rock metamorphic reactions and thus tied to P-T conditions of metamorphic stages [e.g., Parrish, 1990; Foster et al., 2002; Kohn and Malloy, 2004]. We use integrated PTt data from these rocks, and further petrographical evidence from associated mafic rocks to elucidate the tectonic setting and the processes by which the granulites formed and were exhumed to their present-day position.

2. Geological Setting

[7] All four main Himalayan lithotectonic packages are exposed in Bhutan, from the structurally lowest and southernmost Siwaliks, through the Lesser Himalayan Sequence (LHS), the Greater Himalayan Sequence (GHS) and up into the structurally highest and northernmost Tethyan Sedimentary Sequence (TSS) [e.g., Gansser, 1983; Bhargava, 1995]. Compared with a typical simplified cross section through the central Himalayan orogen [Beaumont et al., 2001, and references therein], the Bhutan architecture shows distinct complexities. First, the main structure bounding the top of the GHS, the South Tibetan Detachment (STD), consists of an older outer structure and a younger inner structure [Hollister and Grujic, 2006; Kellett et al., 2009]. The outer STD is preserved at the base of a series of klippen comprising erosional remnants of metasedimentary (Chekha Group) and TSS rocks [Grujic et al., 2002; Kellett et al., 2009]. It is interpreted to have formed during early Miocene top-to-the-

north movement along the STD. The more northerly inner STD (Figures 1b and 1c) separates the main body of the TSS from the GHS and is interpreted as representing the latest stages of ductile and brittle motion along the STD [Kellett et al., 2009].

[8] Second, between the outer and inner STD systems, GHS rocks are deformed by an out-of-sequence, north dipping, thrust sense shear zone, the Kakhang Thrust, which doubles the map-view width of the GHS in central and eastern Bhutan. This shear zone locally places sillimanite-grade migmatites over garnet-staurolite schists interpreted as belonging to the Chekha Formation [Gansser, 1983; Bhargava, 1995; Davidson et al., 1997], and may have been involved in interrupting motion along the STD and the separation of the inner and outer STD strands exposed in Bhutan [Kellett et al., 2009]. The continuation of the Kakhang Thrust east and west of the type locality in central Bhutan remains uncertain although other out-of-sequence thrusts have been identified at similar structural positions along strike (e.g., the Khumbu Thrust in the Everest region [Searle, 1999] and the High Himal Thrust in eastern Nepal [Goscombe et al., 2006]).

[9] Overall, the GHS in Bhutan consists of amphibolite-grade, sillimanite and/or kyanite-bearing paragneisses and orthogneisses [Gansser, 1983; Swapp and Hollister, 1991; Davidson et al., 1997; Daniel et al., 2003] similar to the rock types described from the GHS elsewhere along the Himalayan chain (e.g., review by Hodges [2000]). Early studies found cordierite-bearing rocks in NW Bhutan, suggesting that higher metamorphic grades had been reached in that region [Swapp and Hollister, 1991]. Mapping in NW Bhutan in the region surrounding the village of Laya [Chakungal, 2006] showed that a package of Sil + Grt + Bt + Pl + Kfs + Qtz ± Crd ± Spl migmatitic gneiss (mineral abbreviations after Whitney and Evans [2010]) is overlain by a package of similar gneiss intercalated with augengneiss, quartzite and calc-silicate with minor mafic and ultramafic lenses exposed in the core of a gentle regional E-W trending antiform (Figures 1b and 1c). The nature and precise location of the boundary between these units remains cryptic. To the northeast, a structurally higher package of augengneiss and Miocene leucogranite extends to the base of the inner STD (Figures 1b and 1c). Dykes, sills and irregular lenses of variably sheared Miocene-aged Ms + Tur + Crd ± And leucogranite are also locally exposed [Kellett et al., 2009]. These leucogranites preserve a condensed strain gradient within a ~1 km thick package from undeformed at the base to S/C mylonite at the top.

3. Sample Descriptions

3.1. Mafic Granulitized Eclogites

[10] Mafic layers and boudins, varying in size from the meter to the kilometer scale are exposed in the core of a gentle antiform in NW Bhutan (Figures 1b and 1c). They

Figure 1. (a) Simplified geological map of the Himalayan orogen modified from original map by Guillot et al. [2008], with permission from Elsevier. (b) Geological map of NW Bhutan. (c) Geological cross section across line marked in Figure 1b. Figures 1b and 1c are modified from Chakungal [2006].

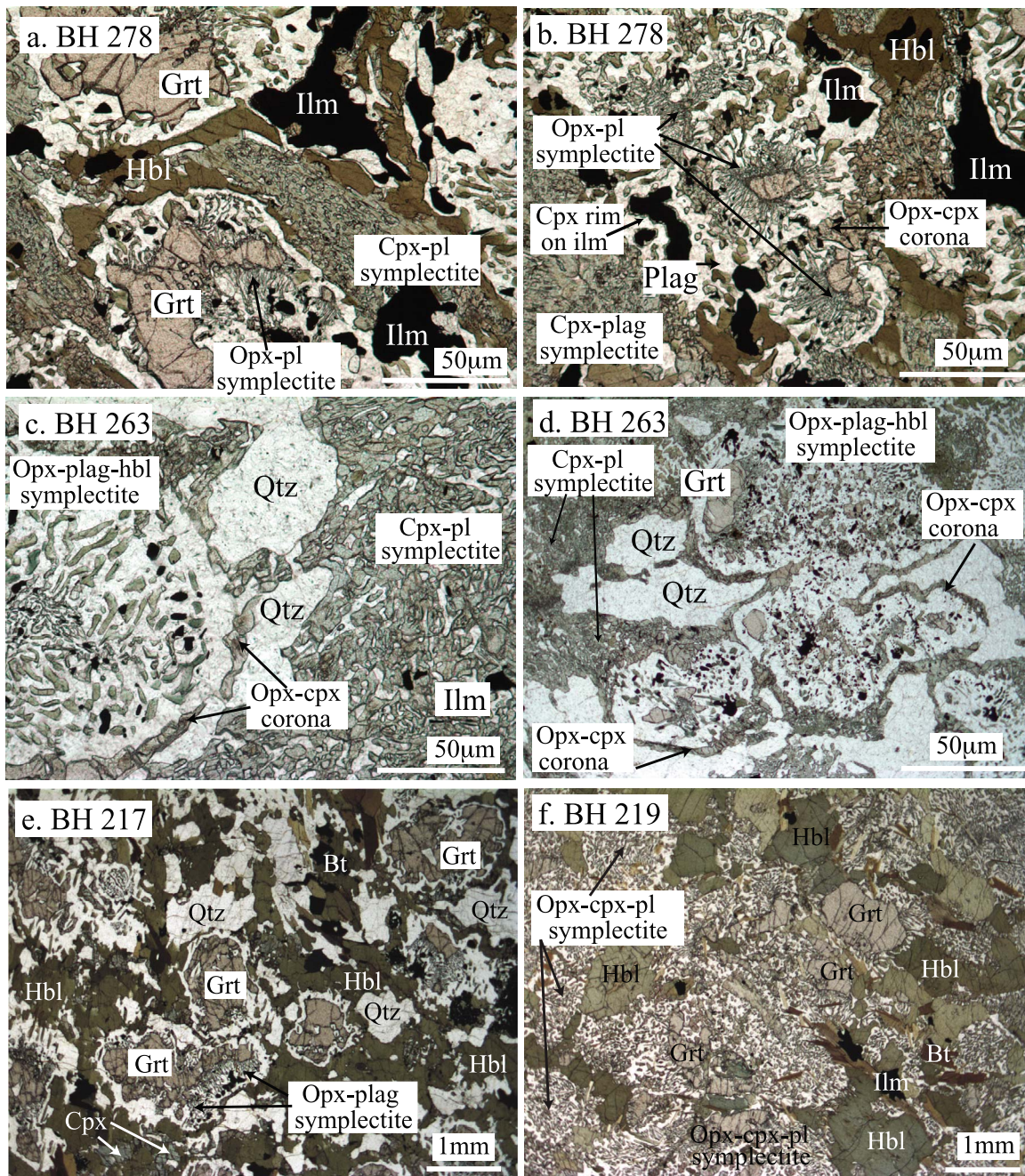


Figure 2. Thin section photomicrographs in plane polarized light of typical mafic granulitized eclogites. Mineral abbreviations after Whitney and Evans [2010].

retain textural evidence for a complex metamorphic evolution (Figure 2 and Chakungal [2006]). Rutile inclusions in garnet, chemical evidence from Cpx + Pl symplectites indicating the presence of precursor omphacite and a lack of evidence for coeval matrix plagioclase all suggest eclogite-facies conditions [O'Brien, 1990; Möller, 1998; Zhao *et al.*, 2000]. This textural evidence for HP metamorphism is now almost completely overprinted by granulite-facies assemblages: coronas of Opx around garnet and clinopyroxene, the breakdown of garnet forming wormy symplectites of

Opx + Pl and Am + Pl, the breakdown of omphacite to form lacy symplectites of Cpx + Pl, and the replacement of rutile by ilmenite (Figure 2 and Chakungal [2006]). These rocks are similar, in texture, mineralogy and composition, to the granulitized eclogites described from Ama Drime in southern Tibet [Lombardo and Rolfo, 2000; Groppo *et al.*, 2007] and nearby Arun Valley in Nepal [Corrie *et al.*, 2010]. The Ama Drime PT path has been suggested to include decompression from HP conditions of >1.5 GPa and >580°C to HT conditions of 0.7–1.0 GPa and ~750°C, followed by final

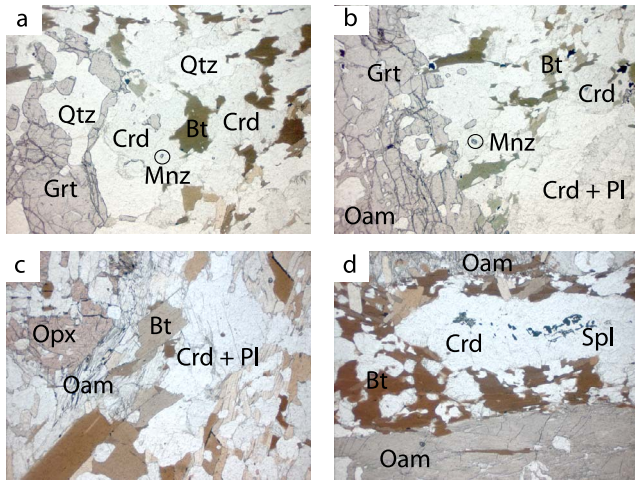


Figure 3. (a-d) Thin section photomicrographs in plane polarized light of pelitic granulite sample BH 243. Mineral abbreviations after *Whitney and Evans* [2010]. Field of view of Figures 3a and 3b is 2.8×2.1 mm and that of Figures 3c and 3d is 5.5×4.1 mm.

decompression to 0.3 GPa at $\sim 630^\circ\text{C}$ [*Rolfo et al.*, 2008; *Lombardo and Rolfo*, 2000; *Groppi et al.*, 2007; *Cottle et al.*, 2009a]. A similar path is inferred for the Bhutan granulitized eclogites (this work and *Chakungal* [2006]).

3.2. Metapelitic Granulites

[11] The mafic rocks are hosted within Opx-bearing paragneiss which preserve evidence for granulite-facies metamorphism overprinted by amphibolite-facies metamorphism. The peak garnet-orthopyroxene assemblage in the paragneiss rules out very high pressures [*O'Brien and Rötzer*, 2003], and no textural or chemical evidence for pregranulite-facies metamorphism is preserved.

[12] Sample BH 243 is compositionally banded on a millimeter-centimeter scale and is variably migmatitic (Figure 3). Melanocratic layers contain Grt + Bt + Opx \pm Oam. Leucocratic layers contain Crd + Pl + Qtz \pm Kfs \pm Spl. Accessory minerals include monazite (included in cordierite-bearing leucosome in BH 243; Figure 3), tourmaline, ilmenite, and magnetite. To our knowledge, this is the first documentation of orthopyroxene in the GHS, although the Crd + Pl + Qtz \pm Kfs \pm Spl assemblage (“sillimanite granulite-facies”) has previously been described from equivalent structural levels in Bhutan [*Gansser*, 1983; *Swapp and Hollister*, 1991; *Davidson et al.*, 1997] and from parts of Sikkim [*Neogi et al.*, 1998; *Ganguly et al.*, 2000]. The attainment of peak metamorphic temperature in the pelitic granulites is represented by the assemblage Grt + Opx + Pl + Rt + Qtz (representative mineral compositions are presented in Table 1). This assemblage suggests conditions of $\sim 800^\circ\text{C}$ and >0.8 GPa [*Carrington and Harley*, 1995]. These conditions are similar to the $\sim 750^\circ\text{C}$ and 0.7–1.0 GPa conditions reported for the granulite-facies overprint on the mafic eclogites in Ama Drime [*Groppi et al.*, 2007; *Cottle et al.*, 2009a].

[13] Evidence for decompression is preserved in the minerals that overprint the granulite-facies assemblage. The migmatitic texture, abundance of K-feldspar and lack of muscovite suggest peak temperatures above the muscovite dehydration melting curve [e.g., *Patino Douce and Harris*, 1998]. Matrix biotite shows embayed edges around cordierite, suggesting incipient melting (Figures 3a and 3d). Locally, cordierite contains delicate undeformed symplectic inclusions of Spl ($\text{Fe}/(\text{Fe} + \text{Mg}) = 0.65$) + Sil, suggesting that cordierite crystallization at least partially postdated deformation (Figure 3d). Cordierite and spinel may have been introduced during decompression during breakdown of garnet + sillimanite at circa 0.3 GPa and $>750^\circ\text{C}$ [*Spear et al.*, 1999]. Orthopyroxene crystals are locally adorned with orthoamphibole-dominated reaction rims involving sheaves of acicular crystals containing numerous FeTi-oxide inclusions (Figure 3c), suggesting hydration during decompression. Elsewhere in the matrix orthoamphibole forms coarser, equant grains associated with patchy intergrowths of biotite and cordierite.

3.3. Granulite-Hosting Gneiss

[14] The majority of the granulite-bearing terrane consists of banded gneiss, with alternating Bt + Sil + Grt melanosomes and Qtz + Pl + Kfs leucosomes (Figure 4a, representative analyses in Table 1). In sample BH 213a, the peak metamorphic assemblage contains Grt + Kfs + Pl + Bt + Sil + Qtz, with finer-grained leucosome and coarser-grained melanosome. In contrast to the pelitic granulites, this sample does not contain Opx or Crd, and does not appear to preserve mineralogical evidence for granulite-facies metamorphism. This sample yields conditions of $\sim 700^\circ\text{C}$ at 0.45 GPa using the conventional Bt-Grt thermometer and GASP barometer compiled by D. J. Waters (spreadsheet “elite.barometers.xls” at http://www.earth.ox.ac.uk/~davewa/pt/th_tools.html). These conditions are similar to those suggested for a biotite-sillimanite-plagioclase-garnet gneiss from the Ama Drime range (sample EV97-60 [*Groppi et al.*, 2007]).

3.4. Laya Valley Gneiss

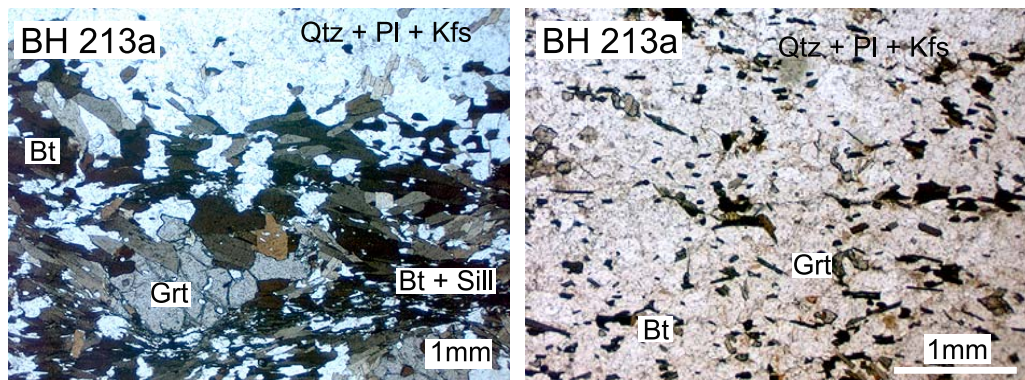
[15] South of the granulite-bearing region, the dominant rock type is also banded migmatitic gneiss with alternating Bt + Sil melanocratic and Qtz + Fsp leucocratic layers (Figure 4b, representative analyses in Table 1). The peak metamorphic assemblage contains Grt + Bt + Kfs + Pl + Sill + Qtz. Cordierite (in sample BH 165) commonly contains inclusions of sillimanite and locally, wormy spinel. Larger equant spinel is also found associated with biotite-sillimanite sheaves and on garnet rims in sample BH 165 (Figure 4b).

[16] Sample BH 167 yields conditions of 650°C at 0.3 GPa using the conventional Bt-Grt thermometer and GASP barometer as detailed above. These conditions are within uncertainty of those reported for the granulite host gneiss above and the Grt-Sill-Bt gneiss from the Ama Drime range (sample EV97-60 [*Groppi et al.*, 2007]). The KFMASH petrogenetic grid published by *Groppi et al.* [2007], suggests that the cordierite and spinel assemblage in sample BH 165 represents decompression to <0.3 GPa at elevated ($>600^\circ\text{C}$) temperatures.

Table 1. Major-Element Mineral Compositions for Representative Samples of the Bhutan Pelitic Granulites and Their Host and Neighboring Gneisses^a

^aMajor-element concentrations were determined using the Dalhousie University JEOL 8200 5-spectrometer and the Open University Cameca SX-100 5-spectrometer Electron Microprobe (EM) using a 10 μm spot size with conditions of 15–20 kV and 20 nA. Natural standards were used for calibration, and a ZAF matrix correction routine was used. Chemical formulas were calculated by stoichiometry. Unknowns were bracketed by analyses of internal secondary standards; uncertainty on major element concentrations is <1%.

a) Granulite host gneiss



b) Laya Valley gneiss

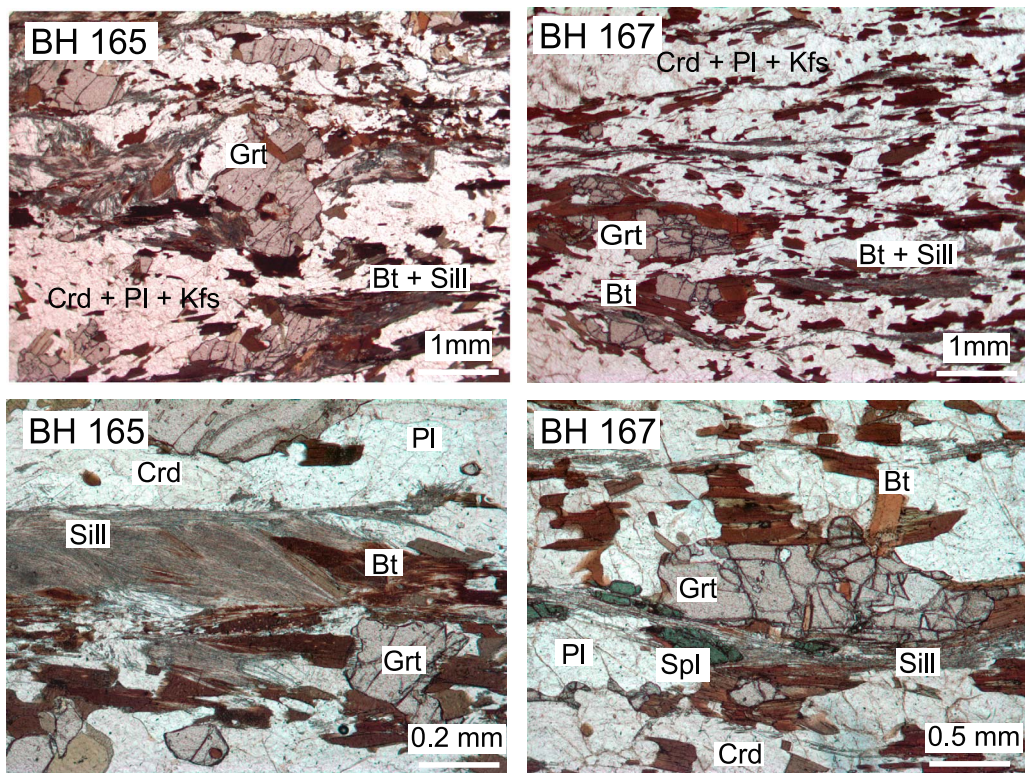


Figure 4. Thin section photomicrographs in plane polarized light. (a) Granulite host gneiss. (b) Granulite absent gneiss from the Laya Valley. Mineral abbreviations after Whitney and Evans [2010].

3.5. Summary

[17] The mafic and pelitic granulites, host gneiss and Laya Valley gneiss are texturally, mineralogically and compositionally similar to reports of granulitized eclogites and their host rocks in Ama Drime [Rollof et al., 2008; Lombardo and Rollof, 2000; Groppo et al., 2007; Cottile et al., 2009a; Kali et al., 2010]. The attainment of plagioclase-absent (eclogite facies) peak pressure conditions is indicated by textures in the mafic rocks, suggesting conditions >1.4 GPa at $\sim 600^{\circ}\text{C}$. Decompression and further heating is indicated by the attainment of granulite facies conditions in both the mafic and

pelitic rocks ($\sim 750^{\circ}\text{C}$ – 800°C , 0.8–1.0 GPa), followed by decompression and cooling to amphibolite facies conditions of $\sim 600^{\circ}\text{C}$ – 650°C and 0.3 GPa. These latter conditions are the peak conditions retained by the Grt-Bt-Sill gneisses which host the granulitized eclogites and which also crop out along the Laya valley.

4. Monazite Geochronology

4.1. U-(Th)-Pb Methods

[18] Monazite was dated by laser ablation multicollector inductively coupled plasma mass spectrometry (LA-MC-

ICP-MS) at the NERC Isotope Geosciences Laboratory, UK. Most monazite was dated *in situ* in polished sections, however monazite separates from four samples (RLB 17, 18, 19 and BH 243) were analyzed in polished epoxy discs. Monazites in all samples were mapped for U, Y, Th, Ce and Nd at 1 μm resolution (100 ms per pixel) on the Open University Cameca SX100 EMP prior to dating in order to identify elemental zoning, assist laser spot location and facilitate age interpretation.

[19] The laser ablation instrumentation consists of a Nu Plasma MC-ICP-MS (Nu Instruments, Wrexham, UK) and a UP193SS laser ablation system (New Wave Research, UK). Detailed instrumental configuration and measurement procedures follow previous methods [Cottle *et al.*, 2009a, 2009b]. Analyses were achieved using a static ablation spot size of 15 μm and a laser fluence of 2–3 Jcm^{-2} (equating to a crater depth of \sim 12 μm). U-Th-Pb data were normalized to the 554 Ma “Manangotry” [Paquette *et al.*, 1994] primary reference monazite. An in-house secondary reference monazite (FC-1, 55.6 \pm 1.3 Ma [Horstwood *et al.*, 2003]) was analyzed concurrently to monitor data accuracy. Overall uncertainties achieved on the secondary reference material were 3% (2 SD) for U-Pb and 4% (2 SD) for Th-Pb data. All quoted uncertainties include contributions from the external reproducibility of the standard for $^{206}\text{Pb}/^{238}\text{U}$, and $^{208}\text{Pb}/^{232}\text{Th}$ ratios.

[20] All data (Table 2) were processed using an in-house spreadsheet calculation routine. Data recording \ll 0.01 mV ^{207}Pb were rejected and data points with >300 cps ^{204}Pb after correction for the isobaric interference of ^{204}Hg were assessed with respect to the contribution of common Pb. Because of their young age, radiogenic Pb signals are generally low ($^{207}\text{Pb} < 0.1$ mV). This resulted in imprecise $^{207}\text{Pb}/^{235}\text{U}$ ages and difficulty in applying common Pb corrections. The data are therefore plotted on Tera-Wasserburg diagrams uncorrected for common Pb, and with an unconstrained upper intercept calculated using Isoplot version 16 September 2008 [Ludwig, 2001]. All uncertainties are quoted at 2σ confidence in the text and Table 2.

[21] When monazite crystallizes it has the potential to incorporate excess ^{230}Th due to an initial U-Th disequilibrium. This results in “excess” ^{206}Pb in young monazite [Schärer, 1984]. Several previous geochronological studies of monazite from similar metamorphic rocks in the Himalaya have demonstrated that in many cases, for the same crystals the $^{206}\text{Pb}/^{238}\text{U}$ ages are consistent with $^{208}\text{Pb}/^{232}\text{Th}$ ages; the latter being unaffected by excess ^{206}Pb [Cottle *et al.*, 2009a, 2009c; Kellett *et al.*, 2010]. We therefore suggest that the likely effect of excess ^{206}Pb on these samples is minor. Nevertheless we recognize the possibility that the ages reported may be overestimated by maximum of circa 0.5 Ma.

4.2. U-(Th)-Pb Results

4.2.1. Granulite-Bearing Terrane: Granulite, Granite, and Banded Gneiss

[22] Monazite in granulite sample BH 243 (Figures 3a, 3b, and 5a) is exclusively included in cordierite in the leucosome. Twelve data points from four monazite grains yield a weighted average $^{208}\text{Pb}/^{232}\text{Th}$ age of 13.9 ± 0.3 Ma

(MSWD = 0.5; Figure 5a and Table 2). Although monazite in this sample is chemically zoned (mainly in Y and Th), there appears to be no consistent relationship between chemical composition and age.

[23] In the granulite-hosting gneiss BH 213a (Figures 4a and 5b and Table 2), monazite is included in garnet rims or associated with intergrown sillimanite + biotite. Ten analyses (not plotted) form a poorly defined discordia line with an upper intercept of circa 550 Ma; these are interpreted as mixing ages between older cores and younger metamorphic rims and were thus rejected from the age calculations. These older cores coincide with zones of higher Y concentration (e.g., grain 6, analyses 3 and 4; Figure 5b), and are within monazite hosted in both garnet rims and the matrix. The majority of the ten Miocene data points from lower-Y rims surrounding the high-Y old cores or in weakly zoned low-Y monazite yield a weighted average age of 13.5 ± 0.5 Ma (MSWD = 0.1; Figure 5b). A further five analyses are slightly older, yielding a weighted average $^{208}\text{Pb}/^{232}\text{Th}$ age of 15.4 ± 0.8 Ma (MSWD 0.4; Figure 5b). It is unclear whether these data record continuous monazite crystallization between these two dates or whether there are two distinct age populations of monazite in this sample; variations in weak chemical zoning in Th and Y do not correlate with age for the Miocene ages (Figure 5b).

[24] Twenty analyses from four monazite grains in granulite host gneiss RLB 19 yield a $^{207}\text{Pb}/^{206}\text{Pb}/^{238}\text{U}/^{206}\text{Pb}$ intercept age of 13.4 ± 0.5 Ma (Figure 5c and Table 2). Strong zoning in Y and Th does not appear to be related to age (Figure 5c). Since these monazites were analyzed from a mineral separate, their textural context was not preserved. The close field location and similar sample description, however, suggest that the rock is very similar to BH 213a. Therefore, based on their identical ages, we suggest that monazite in RLB 19 grew in the same context as in sample BH 213a.

[25] Eleven analyses from five monazites in nearby granite RLB 18 yield a $^{207}\text{Pb}/^{206}\text{Pb}/^{238}\text{U}/^{206}\text{Pb}$ lower intercept age of 12.4 ± 0.3 Ma (MSWD = 0.6; Figure 6 and Table 2). Six analyses were rejected from the age calculation, one due to high levels of common Pb and five due to apparent mixing with an older age domain ($^{206}\text{Pb}/^{238}\text{U}$ ages ranging from 14 to 16 Ma, see spot locations in Figure 6, especially grain 4). These older ages may relate to an extended period of monazite crystallization in the granitic melt or may be the result of inheritance.

4.2.2. Laya Valley Gneiss

[26] Monazite from banded, migmatitic gneiss in the Laya valley is included in garnet rims associated with intergrown sillimanite and biotite, and included in matrix plagioclase. Twelve data points from gneiss CWB 22 yield a $^{207}\text{Pb}/^{206}\text{Pb}/^{238}\text{U}/^{206}\text{Pb}$ intercept age of 21.0 ± 0.6 Ma (MSWD 1.5; Figure 7a and Table 2). A further nine points lie on a discordia line yielding an imprecise upper intercept age of 548 ± 42 Ma (Figure 7a). Three points were rejected due to high common Pb concentrations. Old ages correlate with high Y concentrations in the cores of some grains (e.g., grain 20, analyses 1, 2, 4; Figure 7a); these older grains are found both in the matrix and included in garnet.

Table 2. U-(Th)-Pb Data for the Samples Discussed in the Text

Sample ID	Context	Pb ppm ^a	Th ppm ^b	U ppm ^b	Th/U ^c	$^{207}\text{Pb}/^{206}\text{Pb}$ 2 σ %	$^{208}\text{Th}/^{206}\text{Pb}$ 2 σ %	$^{208}\text{Th}/^{232}\text{U}$ 2 σ %	$^{207}\text{Pb}/^{235}\text{U}$ 2 σ %	$^{208}\text{Th}/^{235}\text{U}$ 2 σ %	Rho	$^{206}\text{Pb}/^{238}\text{U}$ 2 σ abs	$^{207}\text{Pb}/^{235}\text{U}$ 2 σ abs	$^{208}\text{Pb}/^{232}\text{Th}$ 2 σ abs	Age (Ma)
<i>BH 243 Peñiel Granulite (289°6'14.3"N, 089°45'13.5"E, Collected From Serrve)</i>															
<i>BH 243-1</i>															
<i>BH 243-2</i>															
<i>BH 243-3</i>															
<i>BH 243-4</i>															
<i>BH 243-5</i>															
<i>BH 243-6</i>															
<i>BH 243-7</i>															
<i>BH 243-8</i>															
<i>BH 243-9</i>															
<i>BH 243-10</i>															
<i>BH 213A-13-1</i>															
<i>BH 213A-10-3^d</i>															
<i>BH 213A-10-2</i>															
<i>BH 213A-13-2</i>															
<i>BH 213A-10-5</i>															
<i>BH 213A-10-4</i>															
<i>BH 213A-11-3</i>															
<i>BH 213A-11-2^e</i>															
<i>BH 213A-11-4^f</i>															
<i>BH 213A-13-3</i>															
<i>BH 213A-13-4</i>															
<i>BH 213A-13-5a</i>															
<i>BH 213A-11-1</i>															
<i>BH 213A-6-2</i>															
<i>BH 213A-6-4^d</i>															
<i>BH 213A-6-5^d</i>															
<i>BH 213A-9-6^d</i>															
<i>BH 213A-9-4^d</i>															
<i>BH 213A-8-3</i>															
<i>BH 213A-9-5^d</i>															
<i>BH 213A-9-1^d</i>															
<i>BH 213A-6-2^d</i>															
<i>BH 213A-6-4^d</i>															
<i>BH 213A-6-3^d</i>															
<i>BH 213A-9-2^d</i>															
<i>BH 213A-9-3^d</i>															
<i>RLB 19 Granulite Facies Gneiss (28°08'43.6"N, 089°47'55.6"E, in Situ)</i>															
<i>RLB 19-4-3</i>															
<i>RLB 19-4-5</i>															
<i>RLB 19-1-2</i>															
<i>RLB 19-1-4</i>															
<i>RLB 19-4-4</i>															
<i>RLB 19-1-3</i>															

Table 2. (continued)

Sample ID	Context	Pb ppm ^b	Th ppm ^b	U ppm ^b	$^{208}\text{Th}/^{232}\text{U}$ 2 σ %	$^{207}\text{Pb}/^{206}\text{Pb}$ 2 σ %	$^{206}\text{Pb}/^{238}\text{U}$ 2 σ %	$^{207}\text{Pb}/^{235}\text{U}$ 2 σ %	$^{208}\text{Th}/^{235}\text{U}$ 2 σ %	$^{207}\text{Pb}/^{238}\text{U}$ 2 σ abs	$^{206}\text{Pb}/^{238}\text{U}$ 2 σ abs	$^{207}\text{Pb}/^{235}\text{U}$ 2 σ abs	$^{206}\text{Pb}/^{235}\text{U}$ 2 σ abs	$^{207}\text{Pb}/^{232}\text{Th}$ 2 σ abs	Age (Ma)		
RLB19-4-2	2	471	0.0586	3.65	0.00206	5.63	0.01666	6.71	0.84	551.1	39.9	13.3	0.7	16.8	1.1		
RLB19-1-1	2	524	0.0565	3.06	0.00207	5.65	0.01611	6.43	0.88	472.6	33.9	13.3	0.8	16.2	1.0		
RLB19-4-7	2	472	0.0563	3.22	0.00208	5.58	0.01612	6.45	0.87	463.3	35.7	13.4	0.7	16.2	1.0		
RLB19-4-6	3	612	0.0542	2.77	0.00208	5.57	0.01554	6.22	0.90	381.1	31.1	13.4	0.7	15.7	1.0		
RLB19-2-4	3	748	0.0512	2.35	0.00209	5.62	0.01474	6.09	0.92	250.7	27.0	13.4	0.8	14.9	0.9		
RLB19-3-5	2	565	0.0574	2.81	0.00209	5.67	0.01656	6.32	0.90	508.8	30.9	13.5	0.8	16.7	1.0		
RLB19-3-3	2	514	0.0551	3.11	0.00209	5.65	0.01592	6.45	0.88	417.4	34.7	13.5	0.8	16.0	1.0		
RLB19-4-1	2	485	0.0641	3.33	0.00210	5.60	0.01857	6.52	0.86	746.3	35.2	13.5	0.8	18.7	1.2		
RLB19-2-1	3	614	0.0512	2.71	0.00210	5.69	0.01485	6.30	0.90	249.4	31.2	13.5	0.8	15.0	0.9		
RLB19-3-1	2	529	0.0522	3.22	0.00211	5.62	0.01517	6.48	0.87	294.9	36.7	13.6	0.8	15.3	1.0		
RLB19-3-2	2	570	0.0535	2.82	0.00213	5.58	0.01570	6.25	0.89	349.4	31.8	13.7	0.8	15.8	1.0		
RLB19-3-4	4	909	0.0617	2.49	0.00213	5.59	0.01814	6.12	0.91	664.2	26.7	13.7	0.8	18.3	1.1		
RLB19-2-3	3	649	0.0529	2.49	0.00214	5.70	0.01563	6.22	0.92	325.7	28.3	13.8	0.8	15.8	1.0		
RLB19-2-2	2	535	0.0544	2.81	0.00215	5.66	0.01615	6.32	0.90	388.1	31.5	13.9	0.8	16.3	1.0		
RLB 18, Granite, Granulite Zone ($28^{\circ}0'37.7''E, 089^{\circ}47.31.1''N, in Situ$)																	
RLB18-2-4	2	599	0.0584	2.81	0.00190	6.55	0.0153	7.13	0.92	545.2	30.7	12.2	0.8	15.4	1.1		
RLB18-3-3	3	870	0.0548	3.67	0.00191	6.01	0.0144	7.04	0.85	404.9	41.1	12.3	0.7	14.6	1.0		
RLB18-2-3	2	432	0.0674	3.09	0.00193	6.04	0.0180	6.79	0.89	850.1	32.2	12.4	0.8	18.1	1.2		
RLB18-2-1	2	596	0.0592	2.85	0.00194	6.03	0.0159	6.67	0.90	572.6	31.0	12.5	0.8	16.0	1.1		
RLB18-2-2	2	431	0.0683	3.52	0.00197	5.63	0.0186	6.64	0.85	876.8	36.4	12.7	0.7	18.7	1.2		
RLB18-1-1	1	194	0.0751	5.22	0.00202	5.56	0.0209	7.63	0.73	1072.1	52.5	13.0	0.7	21.0	1.6		
RLB18-5-1	1	136	0.0960	6.16	0.00203	5.80	0.0268	8.46	0.69	1546.8	57.9	13.0	0.8	26.9	2.2		
RLB18-1-3	1	221	0.0740	4.91	0.00204	5.60	0.0208	7.44	0.75	1041.8	49.5	13.1	0.7	20.9	1.5		
RLB18-3-2	1	162	0.0930	5.75	0.00210	5.87	0.0269	8.22	0.71	1487.2	54.5	13.5	0.8	26.9	2.2		
RLB18-5-3	1	137	0.0998	5.68	0.00212	5.66	0.0292	8.02	0.71	1619.7	52.9	13.6	0.8	29.2	2.3		
RLB18-5-2	1	148	0.1643	4.41	0.00220	6.11	0.0498	7.53	0.81	250.0	37.1	14.2	0.9	49.4	3.6		
RLB18-1-4 ^d	1	140	0.0658	7.36	0.00221	5.58	0.0200	9.24	0.60	800.1	77.1	14.2	0.8	20.2	1.8		
RLB18-1-2 ^d	0.5	96	0.0730	9.37	0.00230	5.72	0.0231	10.98	0.52	1014.6	94.9	14.8	0.8	23.2	2.5		
RLB18-4-2 ^d	2	487	0.0575	2.71	0.00235	6.47	0.0186	7.01	0.92	511.2	29.8	15.1	1.0	18.7	1.3		
RLB18-4-3 ^d	3	500	0.0546	2.48	0.00257	6.69	0.0194	7.13	0.94	396.2	27.8	16.6	1.1	19.5	1.4		
RLB18-4-1 ^d	3	555	0.0558	3.49	0.00265	6.11	0.0204	7.04	0.87	445.3	38.8	17.1	1.0	20.5	1.4		
RLB18-3-1 ^d	1	93	0.3173	3.86	0.00325	6.44	0.1423	7.51	0.86	3556.9	29.7	20.9	1.3	135.1	9.4		
CWB 22 Laya Valley Granites ($28^{\circ}0'15.4''N, 089^{\circ}33.7.3''E, in Situ$)																	
CWB22_mnz20_3	Pt	277	0.0999	7.34	0.00339	4.22	0.0467	8.47	0.50	1622.1	68.3	21.8	0.9	46.3	3.8		
CWB22_mnz14_2 ^d	Pt	184	0.1793	6.18	0.00341	3.19	0.0844	6.96	0.46	2646.7	51.3	22.0	0.7	82.2	5.5		
CWB22_mnz26_2	Bt	223	0.0965	7.10	0.00346	3.27	0.0460	7.81	0.42	1357.3	66.6	22.3	0.7	45.7	3.5		
CWB22_mnz7_1	Pt	233	0.1024	6.12	0.00351	3.15	0.0496	6.89	0.46	1668.2	56.6	22.6	0.7	49.1	3.3		
CWB22_mnz6_1	Bt	244	0.2856	0.1154	6.22	0.00352	3.34	0.0560	7.06	0.47	1886.8	56.0	22.6	0.8	55.3	3.8	
CWB22_mnz7_2	Pt	240	0.2757	0.1247	7.10	0.00365	3.29	0.0627	7.82	0.42	2024.6	62.8	23.5	0.8	61.8	4.7	
CWB22_mnz5_1	Bt	207	0.2349	0.1121	4.48	0.00365	3.09	0.0564	5.44	0.57	1833.0	40.6	23.5	0.7	55.7	2.9	
CWB22_mnz10_1	Bt	178	0.2006	0.1334	7.57	0.00368	3.28	0.0677	8.25	0.40	2142.8	66.2	23.7	0.8	66.5	5.3	
CWB22_mnz5_1	Pt	174	0.1997	0.1203	6.61	0.00370	4.24	0.0614	7.85	0.54	1960.7	59.0	23.8	1.0	60.5	4.6	
CWB22_mnz9_1	Grt	366	0.4037	0.1510	7.10	0.00374	3.53	0.0779	7.93	0.45	2357.0	60.7	24.1	0.8	76.2	5.8	
CWB22_mnz18	Grt	328	0.2200	9.20	0.00396	5.05	0.1202	10.49	0.48	2980.4	74.0	25.5	1.3	115.2	11.4		
CWB22_mnz14_2	Pt	124	0.1613	6.73	0.00402	5.04	0.0894	8.41	0.60	2469.6	56.8	25.9	1.3	87.0	7.0		
CWB22_mnz5_2	Bt	201	0.1871	0.2422	12.54	0.00451	6.09	0.1506	13.94	0.44	3134.8	99.6	29.0	1.8	142.4	18.4	
CWB22_mnz10_2	Pt	338	0.1249	3.06	0.00550	3.42	0.0948	4.59	0.74	2028.0	27.1	35.4	1.2	92.0	4.0		
CWB22_mnz21_2	Pt	1729	0.3389	0.0697	2.89	0.02117	3.97	0.2035	4.91	0.81	919.7	29.7	135.0	5.3	188.1	8.4	
CWB22_mnz7_1	Bt	918	0.1521	2.54	0.0901	2.54	0.0262	3.64	0.3183	4.44	0.82	1427.7	24.3	163.1	5.9	280.6	10.8
CWB22_mnz21_3	Pt	2505	0.3735	0.0661	4.59	0.02758	3.76	0.2511	5.94	0.63	808.0	48.0	175.4	6.5	227.6	12.0	
CWB22_mnz17_3	Bt	2169	0.3297	0.0686	4.15	0.02296	10.44	0.2644	11.24	0.93	886.3	42.9	177.7	18.3	238.2	23.6	
CWB22_mnz25_2	Bt	2719	0.3559	0.0649	1.55	0.03207	3.64	0.2870	3.96	0.92	771.3	16.3	203.5	7.3	256.2	8.9	
CWB22_mnz17_2	Bt	2743	0.3127	0.0640	0.91	0.03677	3.58	0.3247	3.70	0.97	743.2	9.6	232.8	8.2	285.5	9.2	

Table 2. (continued)

Sample ID	Context	Pb ppm ^b	Th ppm ^b	U ppm ^b	Th/U ^c	207Pb/206Pb 2 σ %	208Th/206Pb 2 σ %	206Pb/238U 2 σ %	207Pb/235U 2 σ %	Rho	208Th/235U 2 σ abs	207Pb/238U 2 σ abs	206Pb/235U 2 σ abs	207Pb/235U 2 σ abs	208Pb/232Th 2 σ abs	Age (Ma)
<i>CWB33 Lay Valley Gneiss (28°04'1.8''N, 089°37'3.0''E, in Situ)</i>																
CWB22_mnz21_1	P1	4576	4302	0.0615	1.43	0.04441	4.04	0.3763	4.29	0.94	655.5	15.3	280.1	11.1	324.3	11.8
CWB22_mnz20_4	P1	2948	2509	0.0614	0.85	0.04839	3.23	0.4096	3.34	0.97	653.0	9.1	304.6	9.6	348.6	9.8
CWB22_mnz20_1	P1	3031	2022	0.0612	0.91	0.06208	3.28	0.5328	3.41	0.96	645.9	9.8	388.3	12.4	427.7	11.8
CWB22_mnz13 ^d	P1	5475	3817	0.0577	0.41	0.06857	21.50	0.5452	21.50	1.00	517.0	4.5	427.5	88.3	441.8	74.2
CWB22_mnz20_2	P1	3652	1900	0.0613	2.05	0.07629	3.80	0.6444	4.32	0.88	648.6	22.1	473.9	17.4	505.1	17.1
CWB22_mnz12	Grt	9168	4739	0.0597	2.26	0.08123	2.98	0.6683	3.74	0.80	591.7	24.5	503.4	14.4	519.7	15.1
<i>BH 165 Lay Valley Gneiss (28°04'1.8''N, 089°37'3.0''E, in Situ)</i>																
CWB33_mnz2_04 ^d	Qz/Kfs/Bt	1249	20221	0.0520	1.94	0.0260	4.63	0.0186	5.03	0.92	285.5	22.2	16.7	0.8	18.7	0.9
CWB33_mnz9_1 ^d	Bt/Kfs	808	12186	0.0590	3.00	0.0270	3.87	0.0220	4.90	0.79	565.8	32.6	17.4	0.7	22.1	1.1
CWB33_mnz2_02 ^d	Qz/Kfs/Bt	1031	15160	0.0553	2.10	0.0281	4.47	0.0214	4.93	0.91	422.5	23.4	18.1	0.8	21.5	1.0
CWB33_mnz9_4	Bt/Kfs	999	14001	0.0549	1.76	0.0289	3.74	0.0219	4.14	0.91	409.8	19.6	18.6	0.7	22.0	0.9
CWB33_mnz9_3	Bt/Kfs	814	11237	0.0559	2.11	0.0295	4.56	0.0227	5.02	0.91	449.0	23.4	19.0	0.9	22.8	1.1
CWB33_mnz6_03 ^d	Bt/Kfs	484	6729	0.0967	2.02	0.0299	4.52	0.0399	4.95	0.91	1561.2	18.9	19.3	0.9	39.7	1.9
CWB33_mnz9_2	Bt/Kfs	706	9521	0.0627	3.42	0.0301	4.51	0.0260	5.66	0.80	696.8	36.4	19.4	0.9	26.1	1.5
CWB33_mnz7_2	Bt/Kfs	1024	13711	0.0486	3.83	0.0307	6.57	0.0206	7.60	0.86	126.8	45.0	19.8	1.3	20.7	1.6
CWB33_mnz7_3	Bt/Kfs	721	9451	0.0556	2.55	0.0310	4.90	0.0238	5.53	0.89	435.6	28.4	20.0	1.0	23.9	1.3
CWB33_mnz7_1	Bt/Kfs	1145	15078	0.0502	2.75	0.0311	3.48	0.0215	4.43	0.78	206.4	31.9	20.0	0.7	21.6	0.9
CWB33_mnz7_5	Bt/Kfs	772	10230	0.0564	2.56	0.0313	5.26	0.0244	5.85	0.90	469.8	28.3	20.2	1.1	24.5	1.4
CWB33_mnz7_4	Bt/Kfs	707	9111	0.0588	2.97	0.0314	5.92	0.0255	6.62	0.89	559.2	32.4	20.2	1.2	25.5	1.7
CWB33_mnz7_6	Bt/Kfs	820	10527	0.0593	2.20	0.0315	6.07	0.0257	6.46	0.94	577.7	23.9	20.2	1.2	25.8	1.6
Kfs	856	11624	0.0801	1.47	0.0318	3.95	0.0351	4.21	0.94	119.9	14.5	20.5	0.8	35.0	1.5	
CWB33_mnz2_03	Qz/Kfs/Bt	794	10310	0.0659	1.93	0.0319	5.16	0.0290	5.51	0.84	804.2	26.2	20.5	1.1	29.0	1.6
CWB33_mnz2_01	Qz/Kfs/Bt	864	11052	0.0832	2.30	0.0322	4.30	0.0370	5.07	0.85	127.3	26.3	20.7	0.9	36.8	1.8
CWB33_mnz9_6	Bt/Kfs	5611	0.0677	4.05	0.0323	4.03	0.0302	5.72	0.71	858.5	42.0	20.8	0.8	30.2	1.7	
CWB33_mnz6_04	Bt/Kfs	709	9025	0.0558	2.33	0.0327	4.16	0.0252	4.76	0.87	445.6	25.8	21.1	0.9	25.3	1.2
CWB33_mnz7_1	Qz/Bt	408	5187	0.0802	2.73	0.0338	3.66	0.0374	7.01	0.80	120.1	26.9	21.8	0.8	37.3	1.7
CWB33_mnz9_5	Bt/Kfs	437	5186	0.0742	2.78	0.0339	3.71	0.0346	4.64	0.80	104.8	28.0	21.8	0.8	34.6	1.6
CWB33_mnz10_2	Qz/Bt	528	6823	0.0987	2.20	0.0344	4.23	0.0468	4.77	0.89	159.8	20.5	22.1	0.9	46.4	2.2
CWB33_mnz41_2	Kfs	295	33668	0.0890	3.29	0.0345	4.05	0.0423	5.22	0.78	1404.6	31.5	22.2	0.9	42.1	2.1
CWB33_mnz6_04	Bt/Kfs	441	5611	0.0677	4.05	0.0323	4.03	0.0302	5.72	0.71	858.5	42.0	20.8	0.8	30.2	1.7
CWB33_mnz10_1	Qz/Bt	708	9025	0.0558	2.33	0.0327	4.16	0.0252	4.76	0.87	445.6	25.8	21.1	0.9	25.3	1.2
CWB33_mnz9_5	Bt/Kfs	437	5186	0.0742	2.78	0.0338	3.66	0.0374	7.01	0.80	120.1	26.9	21.8	0.8	37.3	1.7
CWB33_mnz10_2	Qz/Bt	525	6823	0.0987	2.20	0.0344	4.23	0.0468	4.77	0.89	159.8	20.5	22.1	0.9	46.4	2.2
CWB33_mnz41_2	Kfs	295	33668	0.0890	3.29	0.0345	4.05	0.0423	5.22	0.78	1404.6	31.5	22.2	0.9	42.1	2.1
CWB33_mnz10_3	Qz/Bt	510	4229	0.1161	1.63	0.0508	4.42	0.0814	4.71	0.94	1896.9	14.7	32.7	1.4	79.4	3.6
CWB33_mnz6_06 ^f	Bt/Kfs	781	6633	0.0619	1.94	0.0511	6.74	0.0437	7.01	0.96	670.7	20.7	32.9	2.2	43.4	3.0
CWB33_mnz11_4	Bt	529	4140	0.0647	2.61	0.0538	5.86	0.0480	6.42	0.91	764.3	27.5	34.6	2.0	47.6	3.0
CWB33_mnz11_3	Bt	525	3923	0.0712	2.44	0.0564	7.51	0.0554	7.90	0.95	963.3	24.9	36.2	2.7	54.7	4.2
CWB33_mnz11_1	Bt	918	5065	0.0831	2.09	0.073	4.21	0.0886	4.70	0.90	1272.6	20.4	49.7	2.1	86.2	3.9
CWB33_mnz11_6	Bt	1725	8362	0.0933	0.76	0.0859	7.73	0.1105	7.77	1.00	1494.5	5.1	55.1	4.2	106.4	7.8
CWB33_mnz11_5	Bt	2986	8397	0.0718	0.58	0.01478	6.35	0.1464	6.38	1.00	981.7	5.9	94.6	6.0	138.8	8.2
CWB33_mnz19_2	Bt	2517	5697	0.0611	11.15	0.01855	4.08	0.1563	11.87	0.34	643.8	118.5	4.8	147.5	162	162
CWB33_mnz19_3	Bt	3300	6609	0.0630	5.74	0.02096	5.13	0.1821	7.70	0.67	708.4	13.8	6.8	169.9	12.0	12.0
CWB33_mnz10_5 ^f	Kfs	4341	0.0597	1.36	0.02207	17.54	0.1816	17.59	1.00	592.6	14.7	140.7	24.4	169.5	27.1	27.1
CWB33_mnz27_1 ^d	Kfs	4007	7202	0.0770	33.76	0.02332	10.81	0.2477	35.45	0.31	1121.9	36.6	148.6	5.5	224.7	69.0
CWB33_mnz11_2	Bt	3214	4461	0.0579	6.25	0.03030	3.90	0.2419	7.36	0.53	525.9	68.5	192.4	7.4	220.0	14.5
CWB33_mnz10_4	Qz/Bt	3656	4323	0.0598	3.39	0.03618	5.23	0.2981	6.23	0.84	595.0	36.7	229.1	11.8	264.9	14.4
CWB33_mnz27_2	Kfs	6784	7762	0.0626	8.96	0.03637	4.08	0.3136	9.84	0.41	693.1	95.5	230.3	9.2	277.0	23.6
CWB33_mnz41_1 ^d	Kfs	1460	1004	0.0701	1.04	0.06098	6.49	0.3890	6.57	0.99	930.2	10.7	381.6	24.0	470.3	24.4
CWB33_mnz6_01 ^f	Bt/Kfs	6429	4012	0.0571	0.50	0.06714	5.57	0.5389	5.59	1.00	496.6	5.5	418.9	22.5	431.1	19.4
CWB33_mnz29_1 ^d	Qz	5072	3014	0.0572	16.09	0.07298	5.95	0.5757	17.15	0.35	499.5	177.1	454.1	26.0	461.7	61.7
CWB33_mnz29_2	Qz	4871	2719	0.0582	7.22	0.07595	5.79	0.6100	9.25	0.63	539.2	79.0	471.9	26.3	483.6	35.0
CWB33_mnz6_05	Bt/Kfs	2664	1398	0.0590	0.74	0.07980	3.87	0.6493	3.94	0.98	567.4	8.1	494.9	18.4	508.0	15.6
CWB33_mnz29_3	Qz	2738	1405	0.0622	6.47	0.08027	4.64	0.6880	7.96	0.58	679.7	69.1	497.7	22.2	531.6	32.4
CWB33_mnz19_1	Bt	4074	2098	0.0599	7.02	0.08134	3.45	0.6721	7.82	0.44	600.8	76.0	504.1	16.7	522.0	31.4
165_mn220(2) ^d	B/Sil	282	5002	0.0652	7.46	0.0246	4.25	0.0221	8.59	0.50	780.1	78.4	15.9	0.7	22.2	1.9
165_mnz41_1	Bt	303	4613	0.0653	6.71	0.0292	4.65	0.0263	8.16	0.57	783.8	70.4	18.8	0.9	26.4	2.1

Table 2. (continued)

Sample ID	Context	Pb ppm ^b	Th ppm ^b	U ppm ^b	Th/U ^c	207Pb/206Pb 2 σ %	208Th/206Pb 2 σ %	206Pb/238U 2 σ %	207Pb/235U 2 σ %	208Th/235U 2 σ %	Rho	207Pb/238U 2 σ abs	206Pb/235U 2 σ abs	207Pb/238U 2 σ abs	208Pb/232Th 2 σ abs	Age (Ma)
165_mnz3_001	P1	289	3963	0.0970	5.40	0.00307	4.23	0.0410	6.86	0.62	1566.7	50.6	19.7	0.8	40.8	2.7
165_mnz3_006	P1	241	3299	0.1208	5.21	0.00313	4.35	0.0522	6.79	0.64	1688.7	46.5	20.2	0.9	51.7	3.4
165_mnz1_4	P1	512	6488	0.0660	4.04	0.00328	3.93	0.0299	5.64	0.70	804.9	42.3	21.1	0.8	29.9	1.7
165_mnz1_5	P1	504	6177	0.0770	3.93	0.00331	3.54	0.0351	5.29	0.67	1121.4	39.2	21.3	0.8	35.0	1.8
165_mnz1_1	P1	480	5912	0.0710	5.16	0.00331	3.87	0.0324	6.45	0.60	956.1	52.8	21.3	0.8	32.4	2.1
165_mnz1_2	P1	433	5398	0.0676	4.54	0.00334	4.65	0.0311	6.50	0.72	855.9	47.2	21.5	1.0	31.1	2.0
165_mnz1_3	P1	450	5478	0.0783	3.98	0.00337	3.62	0.0364	5.38	0.67	1154.4	39.5	21.7	0.8	36.3	1.9
165_mnz20a_1	Bt/Sil	156	1994	0.0806	9.68	0.00338	4.33	0.0375	10.61	0.41	1212.8	95.3	21.7	0.9	37.4	3.9
165_mnz1_7	P1	493	5996	0.0684	4.12	0.00338	4.34	0.0319	5.99	0.73	880.0	42.6	21.8	0.9	31.9	1.9
165_mnz1_8	P1	239	2871	0.0965	6.05	0.00343	4.71	0.0457	7.67	0.61	1557.5	56.8	22.1	1.0	45.4	3.4
165_mnz20(2)_1	Bt/Sil	137	1728	0.0975	10.30	0.00344	4.65	0.0462	11.30	0.41	1576.5	96.4	22.1	1.0	45.9	5.1
165_mnz20a_2	Bt/Sil	171	2198	0.1007	8.36	0.00344	4.12	0.0478	9.32	0.44	1637.0	77.6	22.2	0.9	47.4	4.3
165_mnz20a_9	Bt/Sil	196	2468	0.0854	7.73	0.00346	4.24	0.0407	8.81	0.48	1324.9	74.8	22.3	0.9	40.5	3.5
165_mnz20a_10a	Bt/Sil	221	2777	0.0961	8.52	0.00348	4.61	0.0461	9.69	0.48	1549.7	80.0	22.4	1.0	45.8	4.3
165_mnz1_9	P1	252	3037	0.0931	5.81	0.00348	3.30	0.0447	6.68	0.49	1489.7	80.0	22.4	0.7	44.4	2.9
165_mnz1_11	P1	255	2991	0.0965	5.34	0.00350	4.06	0.0465	6.70	0.61	1557.1	50.1	22.5	0.9	46.2	3.0
165_mnz1_10	P1	266	3113	0.0938	5.28	0.00350	3.89	0.0453	6.56	0.59	1504.1	49.9	22.6	0.9	45.0	2.9
165_mnz20a_4	Bt/Sil	144	1786	0.1005	8.96	0.00351	4.15	0.0487	9.88	0.42	1633.9	83.2	22.6	0.9	48.2	4.6
165_mnz20(2)_3	Bt/Sil	160	1979	0.1021	8.93	0.00353	4.44	0.0497	9.97	0.45	1663.2	82.6	22.7	1.0	49.3	4.8
165_mnz20(2)_2	Bt/Sil	138	1689	0.0979	8.84	0.00354	4.51	0.0477	9.93	0.45	1584.4	82.7	22.8	1.0	47.4	4.6
165_mnz1_6 ^d	P1	534	6238	0.1229	2.98	0.00354	5.26	0.0601	6.04	0.87	1999.0	26.4	22.8	1.2	59.2	3.5
165_mnz1_12	P1	248	2868	0.0982	6.27	0.00355	4.70	0.0481	7.84	0.60	1590.2	58.6	22.8	1.1	47.7	3.6
165_mnz1_13	P1	258	2940	0.0925	5.40	0.00356	4.43	0.0454	6.98	0.63	1477.8	51.2	22.9	1.0	45.1	3.1
165_mnz20a_10b ^d	Bt/Sil	311	2842	0.0700	5.93	0.00474	4.32	0.0458	7.33	0.59	928.5	60.9	30.5	1.3	45.5	3.3
165_mnz20a_2 ^d	Bt	260	2245	0.1017	5.90	0.00509	4.99	0.0713	7.73	0.65	1655.6	54.7	32.7	1.6	70.0	5.2
165_mnz20a_3 ^d	Bt/Sil	280	1924	0.0992	7.91	0.00634	4.53	0.0867	9.12	0.50	1608.3	73.8	40.8	1.8	84.5	7.4
165_mnz20a_5 ^d	P1	608	3822	0.4802	6.27	0.00674	8.97	0.0462	10.94	0.82	1481.7	46.4	43.3	3.9	374.6	33.7
165_mnz3_002	P1	758	2464	0.0667	2.99	0.01343	12.86	0.1235	13.20	0.97	828.2	31.2	86.0	11.0	118.3	14.6
165_mnz2_008	P1	2401	6150	0.0594	1.36	0.01688	4.67	0.1382	4.87	0.96	581.2	14.8	107.9	5.0	131.4	6.0
165_mnz3_001	P1	1217	2652	0.0655	2.95	0.01807	7.39	0.1631	7.95	0.93	789.4	30.9	115.5	8.5	153.5	11.3
165_mnz2_009	P1	1926	4229	0.0615	2.19	0.02018	7.34	0.1711	7.15	0.96	1554.4	23.5	128.8	9.4	160.4	11.3
165_mnz2_003	P1	1554	2504	0.0709	4.97	0.02696	5.14	0.2637	7.15	0.72	955.4	50.8	171.5	8.7	237.6	15.0
165_mnz2_005	Bt/Sil	2077	2703	0.0586	1.47	0.03346	5.94	0.2702	6.11	0.97	550.8	16.0	212.2	12.4	242.8	13.1
165_mnz20(2)_6	Bt/Sil	2222	2471	0.0614	1.38	0.03540	4.30	0.2996	4.52	0.95	652.4	14.9	224.3	9.5	266.1	10.5
165_mnz2_008	P1	5447	4807	0.0571	0.83	0.04858	4.26	0.3826	4.34	0.98	496.1	9.2	305.8	12.7	329.0	12.1
165_mnz3_003	P1	3237	2606	0.0625	1.47	0.05226	4.31	0.4590	4.55	0.95	691.6	15.7	334.5	14.0	383.6	14.4
165_mnz2_002	P1	4425	3237	0.0574	0.72	0.05809	7.98	0.4596	8.01	1.00	506.0	7.9	364.0	28.2	384.0	25.3
165_mnz4_3	Bt	3191	1699	0.0595	1.90	0.08286	4.50	0.6800	4.88	0.92	586.1	20.6	513.2	22.1	526.8	19.9
165_mnz2_007	P1	3772	1921	0.0584	0.94	0.08469	4.09	0.6825	4.20	0.97	546.4	10.2	528.3	17.1	528.3	20.6
165_mnz20a_8	Bt/Sil	3867	1968	0.0589	1.78	0.08541	4.23	0.6939	4.58	0.92	564.3	19.4	528.4	21.4	535.2	18.9
165_mnz20a_7	Bt/Sil	2959	1505	0.0590	1.02	0.08619	4.08	0.7009	4.20	0.97	566.5	11.1	532.9	20.8	539.3	17.4
165_mnz20a_6	Bt/Sil	3777	1883	0.0580	0.97	0.08674	4.13	0.6931	4.24	0.97	528.1	10.6	536.2	21.2	534.7	17.5
<i>BH 167 Lay Valley Gneiss (28°3'47.2"N, 89°40'15.2"E, in Situ)</i>																
BH167-9-2 ^d	Bt	201	2997	0.1357	12.45	0.00280	6.34	0.0523	13.97	0.45	2172.8	108.5	18.0	1.1	51.8	7.0
BH167-11-1 ^d	Qz	342	4654	0.0728	2.59	0.00300	1.78	0.0301	3.14	0.57	1007.5	26.2	19.3	0.3	30.1	0.9
BH167-11-2	Qz	364	4857	0.0736	2.47	0.00309	1.71	0.0314	3.01	0.57	1030.8	25.0	19.9	0.3	31.4	0.9
BH167-11-8 ^d	Qz	366	4799	0.0984	2.67	0.00313	1.79	0.0425	3.22	0.56	1593.8	25.0	20.2	0.4	42.2	1.3
BH167-11-6	Qz	361	4661	0.0879	6.89	0.00316	1.79	0.0384	7.12	0.25	1381.3	66.2	20.4	0.4	38.2	2.7
BH167-11-3	Qz	369	4778	0.0748	2.33	0.00318	1.81	0.0328	2.95	0.61	1063.0	23.4	20.5	0.4	32.8	1.0
BH167-11-7	Qz	395	5144	0.0719	2.35	0.00318	1.88	0.0315	3.01	0.63	983.1	23.9	20.5	0.4	31.5	0.9
BH167-11-5	Qz	334	4266	0.0788	2.51	0.00319	1.88	0.0346	3.14	0.60	1166.1	24.9	20.5	0.4	34.6	1.1
BH167-11-8-1	Qz	226	2871	0.0892	3.15	0.00324	1.69	0.0399	3.58	0.47	1408.9	30.2	20.9	0.4	39.7	1.4
BH167-18-4	Qz	233	2946	0.1128	3.43	0.00329	2.93	0.0512	4.51	0.65	1844.4	31.0	21.2	0.6	50.7	2.2
BH167-11-4	Qz	354	4416	0.0896	2.24	0.00330	2.05	0.0407	3.04	0.67	1417.9	21.4	21.2	0.4	40.5	1.2

Table 2. (continued)

Sample ID	Context	Pb ppm ^b	Th ppm ^b	U ppm ^b	Th/U ^c	207Pb/206Pb 2σ %	208Th/206Pb 2σ %	206Pb/238U 2σ %	207Pb/235U 2σ %	208Th/232U 2σ %	Rho	Age (Ma)				
												206Pb/238U 2σ abs	207Pb/235U 2σ abs	206Pb/235U 2σ abs	207Pb/232Th 2σ abs	
BH167-16-1 ^d	Bi	178	2101	0.1092	3.55	0.00352	1.61	0.0529	3.90	0.41	1785.5	32.4	22.6	0.4	52.4	2.0
BH167-16-3	Bi	208	2310	0.1589	2.30	0.00374	1.85	0.0819	2.95	0.63	2443.5	19.4	24.1	0.4	80.0	2.3
BH167-8-3	Qz	3300	2985	0.0605	0.86	0.04392	10.57	0.3330	10.60	1.00	621.3	9.2	289.4	29.8	329.2	29.4
BH167-18-1 ^d	Qz	2987	2531	0.0655	2.57	0.04714	16.62	0.4259	16.81	0.99	791.1	26.9	297.0	48.0	360.2	49.8
BH167-18-5	Qz	4011	2863	0.0615	0.48	0.05647	5.20	0.4786	5.22	1.00	655.9	5.2	354.1	17.9	397.1	17.0
BH167-18-6	Qz	5510	3654	0.0619	0.37	0.06202	3.09	0.5289	3.11	0.99	668.9	3.9	387.9	11.6	431.1	10.9
BH167-8-2a	Qz	4871	3154	0.0591	0.36	0.06364	1.90	0.5189	1.93	0.98	572.4	7.3	397.7	7.3	424.4	6.7
BH167-10-2	Bi	5287	3356	0.0609	0.30	0.06590	1.70	0.5538	1.73	0.98	637.3	3.3	411.4	6.8	447.5	6.2
BH167-8-2b	Qz	4977	2965	0.0604	0.66	0.06984	1.83	0.5820	1.94	0.94	619.3	7.1	435.2	7.7	465.7	7.2
BH167-18-2 ^d	Qz	4715	2604	0.0657	0.47	0.07468	3.33	0.6767	3.36	0.99	797.7	5.0	464.3	14.9	524.8	13.7
BH167-15-1	Grt	8320	4561	0.0584	0.25	0.07475	1.87	0.6021	1.89	0.99	545.8	2.7	464.7	8.4	478.6	7.2
BH167-15-2	Grt	7434	4065	0.0582	0.36	0.07506	1.88	0.6018	1.92	0.98	535.6	4.0	466.6	8.5	478.4	7.3
BH167-15-3	Grt	6077	3157	0.0592	0.62	0.07913	2.26	0.6463	2.34	0.96	575.8	6.7	490.9	10.7	506.2	9.3
<i>RLB 16, Granites, South of Lava Valley (28°0'12.7"E, 28°43'42.5"N, in Situ)</i>																
RLB16-5-3	2	379	0.0470	4.13	5.59	0.0164	6.95	0.80	47.9	49.4	16.4	0.9	16.6	1.1		
RLB16-4-4	2	365	0.0481	3.91	5.59	0.00254	5.63	0.0172	6.85	0.82	105.6	46.2	46.6	0.9	17.3	1.2
RLB16-4-3	2	388	0.0473	3.71	5.64	0.00262	5.64	0.0171	6.75	0.84	63.4	44.2	44.8	0.9	17.2	1.1
RLB16-5-2	2	408	0.0454	3.56	5.59	0.00266	5.59	0.0167	6.63	0.84	32.9	43.2	17.1	1.0	16.8	1.1
RLB16-5-1 ^d	2	412	0.0571	2.92	5.60	0.00268	5.60	0.0211	6.32	0.89	494.9	32.2	17.3	1.0	21.2	1.3
RLB16-4-2	2	403	0.0462	3.49	5.60	0.00270	5.60	0.0172	6.60	0.85	8.8	42.0	17.4	1.0	17.3	1.1
RLB16-4-1	2	406	0.0456	3.38	5.58	0.00278	5.58	0.0175	6.53	0.86	-23.0	41.0	17.9	1.0	17.6	1.1
RLB16-5-4	2	323	0.0444	4.48	5.60	0.00285	5.60	0.0174	7.18	0.78	-90.5	55.0	18.4	1.0	17.6	1.2
RLB16-2-4 ^d	1	246	0.0562	4.29	5.71	0.00287	5.71	0.0222	7.14	0.80	458.4	47.5	18.5	1.1	22.3	1.6
RLB16-2-2	2	286	0.0466	4.34	5.69	0.00291	5.69	0.0187	7.15	0.79	29.0	52.0	18.7	1.1	18.8	1.3
RLB16-3-1	2	249	0.0473	4.79	5.59	0.00296	5.59	0.0193	7.36	0.76	64.7	57.0	19.0	1.1	19.4	1.4
RLB16-7-4	1	235	0.0476	4.93	5.62	0.00301	5.62	0.0198	7.47	0.75	79.6	58.5	19.4	1.1	19.9	1.5
RLB16-9-3 ^d	1	127	0.0474	6.05	5.60	0.00302	5.71	0.0309	8.32	0.69	1052.0	60.9	19.4	1.1	30.9	2.5
RLB16-3-2	2	269	0.0469	4.62	5.58	0.00302	5.58	0.0195	7.25	0.77	42.5	55.3	19.4	1.1	19.6	1.4
RLB16-9-4 ^d	1	130	0.0749	5.55	5.66	0.00302	5.66	0.0312	7.93	0.71	1066.8	55.7	19.5	1.1	31.2	2.4
RLB16-7-1	2	263	0.0458	5.06	5.59	0.00303	5.59	0.0192	7.54	0.74	-12.1	61.1	19.5	1.1	19.3	1.4
RLB16-2-1	2	282	0.0451	4.77	5.63	0.00304	5.63	0.0189	7.38	0.76	-50.9	58.0	19.5	1.1	19.0	1.4
RLB16-7-3	2	246	0.0460	5.10	5.60	0.00304	5.60	0.0193	7.57	0.74	-2.3	61.5	19.6	1.1	19.4	1.5
RLB16-3-3	2	267	0.0464	4.37	5.61	0.00304	5.61	0.0194	7.11	0.79	15.9	52.5	19.6	1.1	19.6	1.4
RLB16-7-2	2	261	0.0459	4.82	5.59	0.00305	5.59	0.0193	7.38	0.76	-6.8	58.1	19.6	1.1	19.4	1.4
RLB16-2-3	2	248	0.0445	4.87	5.85	0.00305	5.85	0.0187	7.61	0.77	-82.6	59.6	19.6	1.1	18.8	1.4
RLB16-3-4	2	251	0.0451	4.80	5.63	0.00306	5.63	0.0190	7.39	0.76	-50.8	58.4	19.7	1.1	19.1	1.4
RLB16-9-2 ^d	1	212	0.0499	5.42	5.78	0.00307	5.78	0.0211	7.93	0.73	188.3	63.1	19.8	1.1	21.2	1.7
RLB16-9-1 ^d	0.5	77	0.0755	9.14	5.82	0.00308	5.82	0.0320	10.83	0.54	1082.4	91.6	19.8	1.2	32.0	3.4

^aThe context column indicates the major mineral textural association of monazite. RLB samples were analyzed in grain mounts with no textural information available.^bU, Th, and Pb contents accurate to approximately 10%.^cNormalized to Th/U ratio of the standard.^dAnalysis that was rejected from final age determination. See text for explanation.

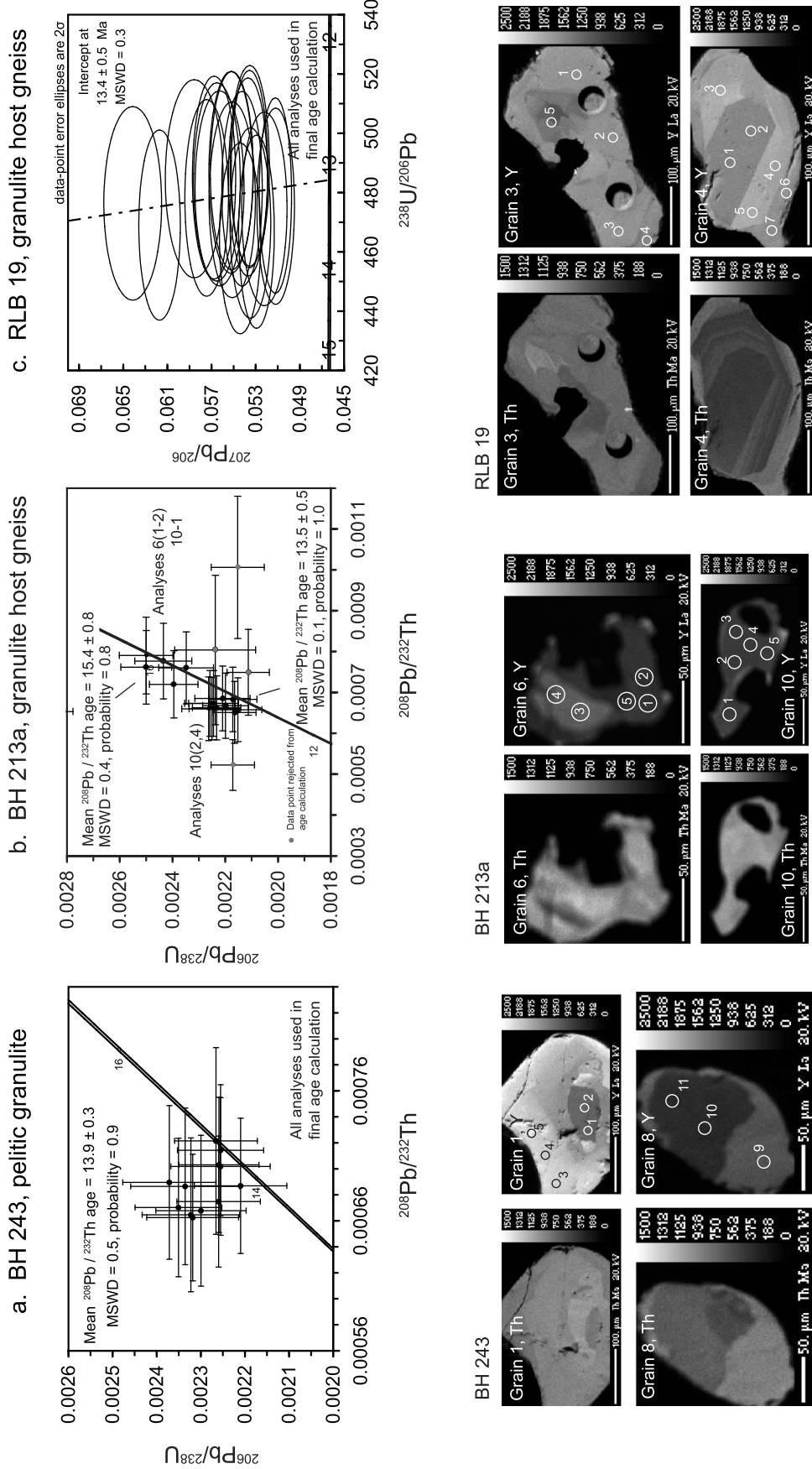


Figure 5. (a, b) Th-Pb diagrams for pelitic granulite BH 243 and granulite host gneiss BH 213a. (c) Tera-Wasserburg U-Pb diagram for granulite host gneiss RLB 19. Chemical maps of Th and Y zoning in selected grains are also presented, including analytical spot locations (data in Table 2). The imaged grain analyses are labeled on the U-Pb diagram. The gray scale on each element map is the same and matches the scale in Figures 6–9.

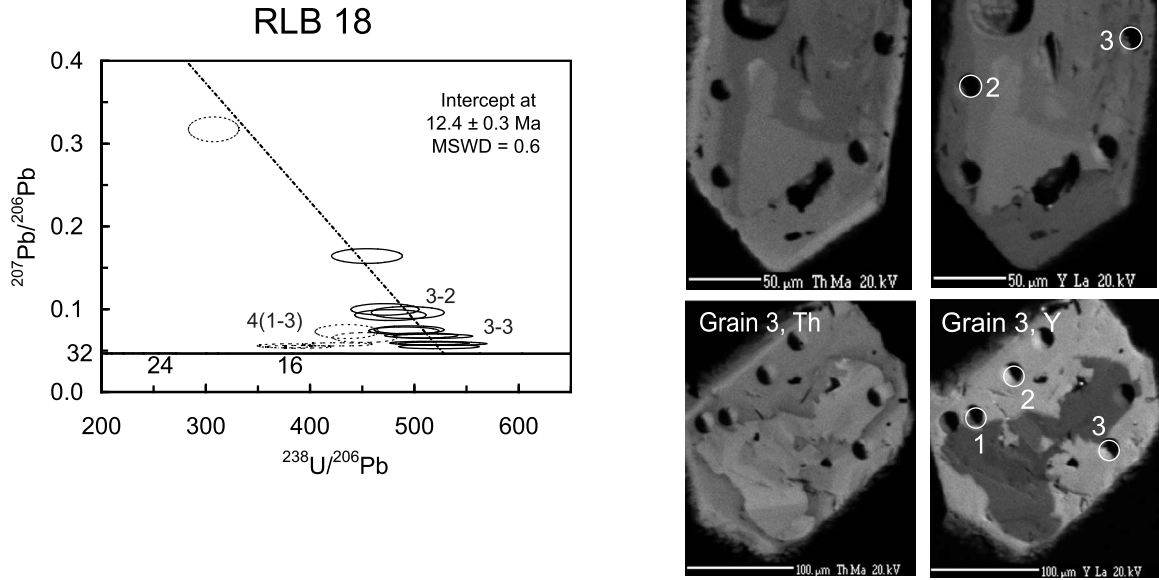


Figure 6. Tera-Wasserburg U-Pb diagram for granite sample RLB 18 and chemical maps of selected grains showing zoning in Th and Y, as well as locations of analytical spots (data in Table 2). The imaged grain analyses are labeled on the U-Pb diagram. The gray scale on each element map is the same and matches the scale in Figures 5, 7, 8, and 9. Equivalent data points are labeled on the TW diagram. Data point error ellipses are 2σ .

[27] Seventeen data points from gneiss CWB 33 yield a spread of data with a $^{207}\text{Pb}/^{206}\text{Pb}$ / $^{238}\text{U}/^{206}\text{Pb}$ intercept age of 19.0 ± 0.7 Ma (MSWD 2.7; Figure 7b and Table 2). Three younger (circa 17 Ma) data points may record a younger (re-)crystallization event; however there is no strong link between variation in Miocene ages and chemical zoning. Monazite cores yield a discordant spread with a $^{207}\text{Pb}/^{235}\text{U}$ / $^{206}\text{Pb}/^{238}\text{U}$ upper intercept age of 583 ± 51 Ma. These Neo-Proterozoic to Cambrian ages are linked to zones of higher Y concentration (Figure 7b).

[28] The majority of twenty nine data points from five matrix monazite grains in gneiss BH 165 are slightly discordant, displaying linear arrays indicative of variable minor components of common Pb (Figure 8 and Table 2). Twenty analyses yield a distinct array with a $^{207}\text{Pb}/^{206}\text{Pb}$ / $^{238}\text{U}/^{206}\text{Pb}$ lower intercept age of 20.5 ± 0.6 Ma (MSWD 0.4). A further three analyses yield a younger age of 18.5 ± 1.1 Ma (MSWD 0.1). No correlation is seen between Th and Y zoning patterns or spot location with respect to the grain rim, and the yielded Miocene age. One distinctly younger analysis (Figure 8), not included in the age calculations above, hints that there may have been monazite crystallization as recently as circa 15 Ma. Fifteen core analyses (linked to high Y concentration) yield a spread along a discordia line, with five analyses yielding a concordant weighted average upper intercept age of circa 536 Ma.

[29] Nine analyses from six monazite grains in the matrix and in garnet in gneiss BH 167 yield a moderately defined intercept age of 19.2 ± 0.5 Ma (MSWD 2.4, four data points

rejected, two of which may indicate monazite growth at a later stage; Table 2). There appears to be no link between Miocene age and chemical zoning patterns (Figure 8). Nine points lie along a discordia line yielding a poorly constrained upper $^{207}\text{Pb}/^{235}\text{U}$ / $^{206}\text{Pb}/^{238}\text{U}$ intercept age of 599 ± 45 Ma; these older ages are linked to zones of high Y concentration.

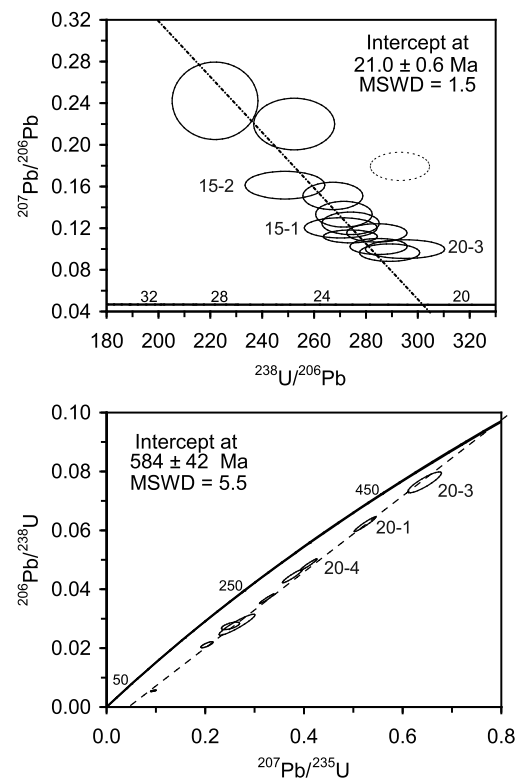
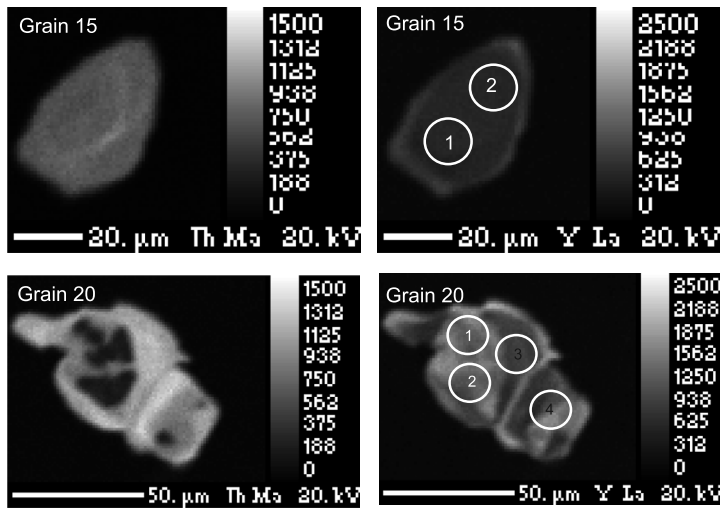
[30] Ten out of 24 data points from monazite rims in gneiss RLB 16 yield a weighted average $^{206}\text{Pb}/^{238}\text{U}$ age of 19.5 ± 0.3 Ma (MSWD 0.7), a further five points yield a younger age of 16.9 ± 0.4 Ma (MWD 0.1; Figure 9 and Table 2). Both sets of ages were obtained from grains with similar zoning patterns (Figure 9); it remains unclear whether monazite crystallized over an extended period of time or whether there were two distinct monazite growth stages. Two points yield ages between the two end-member ages; these were rejected from the end-member age calculations as they may represent mixing between two end-member age domains. A further six discordant points were also rejected from the calculations. Miocene ages do not appear to be linked to minor chemical zoning in Y and Th (Figure 9: grains 3 and 5 appear to have similar Y and Th concentrations yet grain 3 yields the older age and grain 5 the younger age).

5. Discussion and Tectonic Implications

5.1. Timing of Monazite Growth

[31] Monazite in cordierite-bearing leucosome in the pelitic granulites suggests that crystallization at 13.9 ± 0.3 Ma

a. CWB 22



b. CWB 33

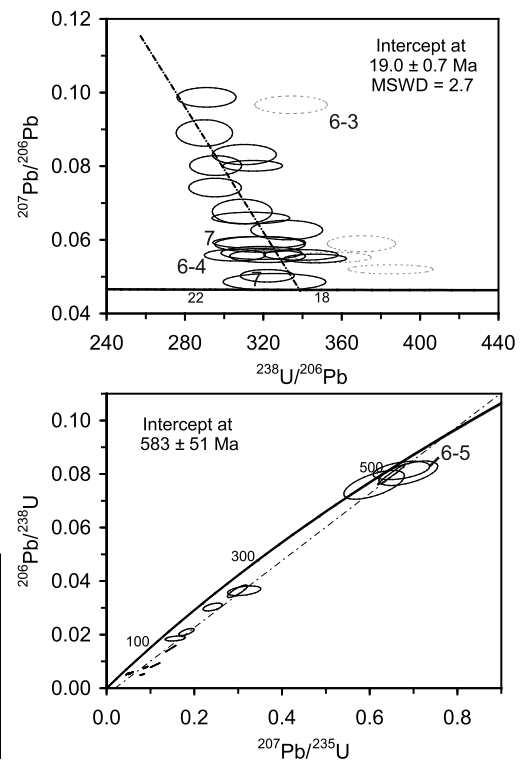
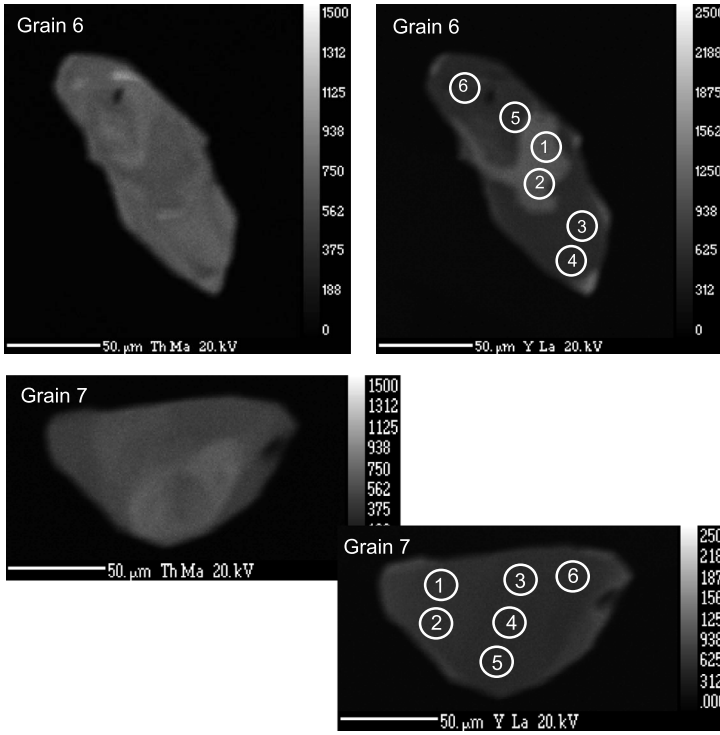


Figure 7. (a and b) Chemical maps showing element zoning in Th and Y in monazite from gneiss samples CWB 22 and CWB 33 from the Laya Valley (Figure 1b) including spot locations (data in Table 2). The imaged grain analyses are labeled on the U-Pb diagrams. Miocene U-Pb monazite data are plotted on Tera-Wasserburg diagrams and Cambro-Ordovician core data are plotted on concordia diagrams. Data point error ellipses are 2σ . The gray scale on each element map is the same and matches the scale in Figures 5, 6, 8, and 9.

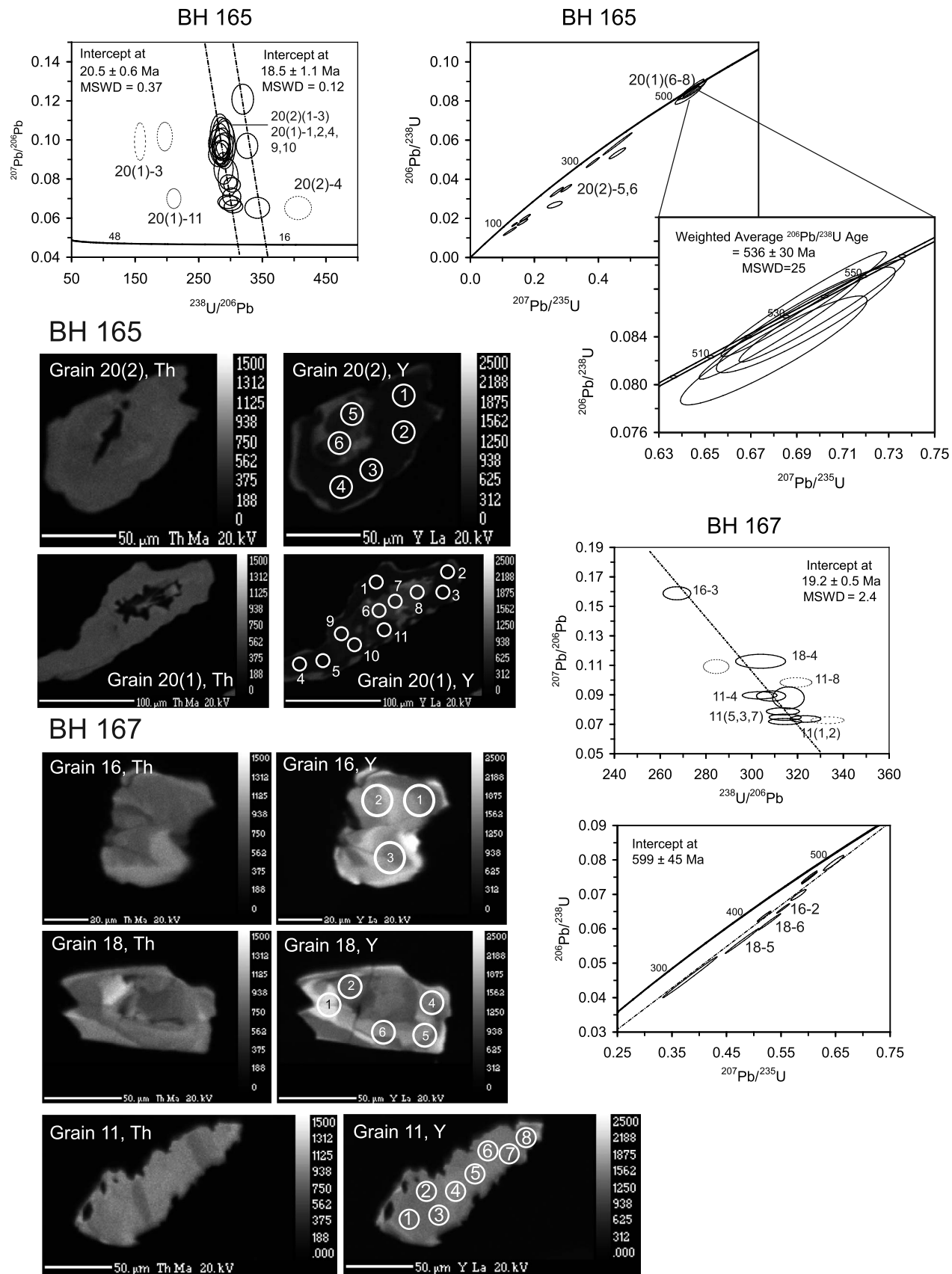


Figure 8

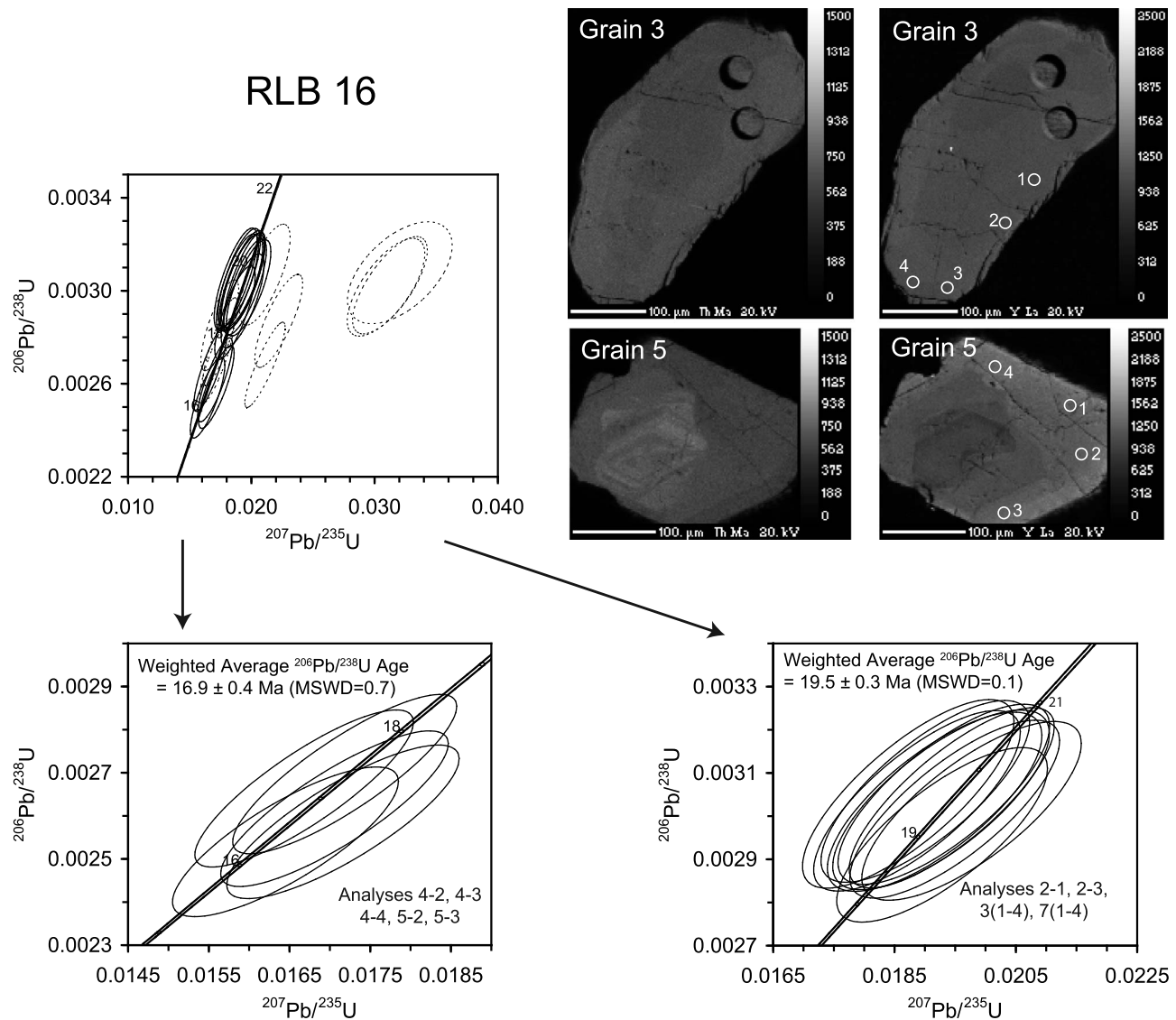


Figure 9. U-Pb concordia diagram for monazite from gneiss RLB 16 and chemical maps of selected grains showing zoning in Th and Y, as well as locations of analytical spots for comparison with Table 2. The imaged grain analyses are labeled on the U-Pb diagram.

coincided with cooling following anatexis [Kelsey et al., 2008]. Monazite included in garnet and associated with Sill + Bt mats in the granulite-hosting gneiss yields ages between 15.4 ± 0.8 Ma and 13.4 ± 0.5 Ma suggesting either two distinct episodes of monazite crystallization at this time or continuous crystallization during cooling. These ages are similar to 13.4 ± 1.0 to 11.0 ± 3.3 Ma U-Th-Pb ages of monazite and xenotime from paragneisses and orthogneisses in Ama Drime, interpreted as constraining the timing of melt

crystallization following granulite-facies metamorphism [Liu et al., 2007; Cottle et al., 2009a; Kali et al., 2010].

[32] Monazite rims from a granite in the granulite terrane yield ages of 12.4 ± 0.3 Ma, suggesting slightly later crystallization of monazite in large granite bodies than in the surrounding migmatites. These data are consistent with previously published data from nearby granites: 15–11 Ma U-Pb SHRIMP zircon rim ages from the top of the GHS, closer to the inner STD, along the same valley [sample BH 225, Kellett et al., 2009], $12.1\text{--}11.6$ Ma $^{207}\text{Pb}/^{235}\text{U}$ TIMS

Figure 8. Chemical maps showing element zoning in Th and Y in monazite from gneiss BH 165 and BH 167 from the Laya Valley (Figure 1) including spot locations for comparison with Table 2. The imaged grain analyses are labeled on the U-Pb diagrams. Miocene U-Pb monazite data are plotted on Tera-Wasserburg diagrams, and Paleozoic core data are plotted on concordia diagrams. Data point error ellipses are 2σ .

monazite ages from a granite further north at Wagye La [Wu et al., 1998] and a 12.5 ± 0.4 Ma Th-Pb SIMS monazite age from the Khula-Kangri granite at the Bhutan-Tibet border [Edwards and Harrison, 1997]. Andalusite reported in granite sample BH 225 suggests low-pressure conditions ($P \leq 2.8$ kbar) during crystallization at this time [Kellett et al., 2009].

[33] Monazite in the gneiss outcropping in the Laya valley yields an array of significantly older 21.0 ± 0.6 to 16.9 ± 0.4 Ma crystallization ages. In addition, granites south of Laya yield zircon crystallization ages of 24–18 Ma [Carosi et al., 2006]. These ages are comparable with a 22 ± 1 Ma U-Pb TIMS monazite age from a St + Ky schist and 18–14.5 Ma TIMS monazite and xenotime ages from deformed leucogranites and Ky + Grt migmatites at the lowest levels of the GHS in SE Bhutan [Daniel et al., 2003].

[34] Together these data suggest that the rocks now exposed at the structurally highest levels of the GHS in NW Bhutan were affected by partial melting and high-temperature recrystallization during decompression from at least granulite-facies conditions during the mid-Miocene, with textural evidence in associated mafic rocks for earlier higher-pressure conditions. The contrast between older ages to the south and younger ages to the north suggest the presence of a major structure separating a younger, structurally higher, cryptic eclogite- and granulite-bearing terrane from an older, structurally lower, granulite-free terrane. The nature of this boundary has important implications for the tectonic history of NW Bhutan.

[35] A high strain zone identified in the field immediately above Laya, and above the trail leading to the west of it, may be the trace of a north dipping, top-to-the-south, thrust which has emplaced granulite-facies gneiss over amphibolite-facies gneiss (Figures 1b and 1c); further detailed mapping and sampling are needed to confirm this. This “Laya Thrust” (Figures 1b and 1c) may be the westward extension of the out-of-sequence Kakhtang Thrust [Gansser, 1983], thought to have been active between 14 and 10 Ma in central Bhutan [Grujic et al., 2002]. This thrust, in conjunction with leucogranite intrusion and tectonic denudation along the inner STDS until at least 11 Ma, may have partially or fully accommodated the rapid isothermal exhumation of the granulites from >1.0 to circa 0.6 GPa at or shortly before 15–13 Ma, and juxtaposed these rocks over Grt-Sill-Bt gneiss in which monazite crystallized between 21 and 17 Ma. This tectonic event may be related to the reorganization of the STDS and the shift of the top-to-the-north shearing from the Outer to the Inner STDS [Kellett et al., 2009].

5.2. Exhumation of the Granulite-Bearing Unit

[36] Textural evidence from mafic rocks exposed in NW Bhutan (Figure 2) suggest that eclogite facies conditions were reached prior to decompression and heating to granulite facies conditions. Exhumation of deeply buried rock may be driven by buoyancy, tectonics, surface erosion, or a combination of these [England and Molnar, 1990; Platt, 1993; Ernst et al., 1997; Ring et al., 1999]. There are several lines of evidence which suggest that different tectonic regimes and exhumation mechanisms are responsible for the

formation and exhumation of HP (greater than circa 1.4 GPa) rocks across the Himalayan orogen [e.g., Guillot et al., 2008]. The driving force responsible for the exhumation of UHP (greater than circa 2.6 GPa) terranes in the NW Himalaya is considered to be buoyancy [e.g., Ernst et al., 1997] as the thinned Indian continental margin was subducted beneath Asia during the earliest stages of continental collision [e.g., de Sigoyer et al., 2000; Leech et al., 2005; Parrish et al., 2006; Guillot et al., 2008]. Evidence for this includes the age of peak metamorphism (within circa 10 Ma of India-Asia collision [Rowley, 1996, 1998; Zhu et al., 2005]), the depth of subduction (pressures of >2.7 GPa equating to depths >95 km assuming an average crustal density of 2800 kg m^{-3}), their structural position immediately beneath (and south of) the India-Asia suture, and the amphibolite-facies overprint during exhumation [e.g., Leech et al., 2005; Parrish et al., 2006; Epard and Steck, 2008]. A quantitative model linking the structural setting and PT evolution of these UHP rocks to their buoyancy-controlled exhumation was recently presented by Beaumont et al. [2009].

[37] In contrast, the eastern Himalayan eclogites appear to have formed 20–25 Ma later, reached HP rather than UHP conditions (no coesite reported), are exposed within the metamorphic core of the Himalaya (GHS and/or LHS) hundreds of kilometers south of the suture, experienced a granulite-facies overprint during exhumation, and are much smaller in volume [Lombardo and Rolfo, 2000; Groppo et al., 2007; Cottle et al., 2009a; Kali et al., 2010; Corrie et al., 2010]. Their recent, circa 21 Ma [Corrie et al., 2010], formation in, and rapid exhumation from, a steep, relatively cold collision-related subduction channel is incompatible with present-day seismic observations of south Tibetan and Himalayan crust [Nelson et al., 1996; Hauck et al., 1998], and would suggest extreme diachroneity of the India-Asia collision which is inconsistent with other available geological data [Rowley, 1996, 1998; Zhu et al., 2005] and plate reconstructions [e.g., Molnar and Stock, 2009]. Buoyancy-related exhumation in a relatively cold geothermal regime is also inconsistent with the observed high-temperature granulite-facies overprint, and is difficult to reconcile with coeval motion on the MCT and STD since circa 22 Ma (see review in the work of Godin et al. [2006]). Formation of the eastern Himalayan HP rocks deep within thickened orogenic crust (crustal thicknesses of ~ 70 – 80 km under southern Tibet equates to pressures of circa 2.0 GPa) is more easily reconcilable with the available geological and geophysical data. Buoyancy cannot be the driving force behind exhumation as no buoyancy difference between the predominantly felsic exhuming rocks and the rest of the (assumed predominantly felsic) lower crust existed at the time of exhumation initiation. The older UHP eclogites found in the western Himalaya and the younger granulite-overprinted lower P eclogites found in the eastern Himalaya therefore formed and exhumed within different tectonic and kinematic regimes.

[38] The structural, metamorphic and geochronological constraints on the mechanism responsible for exhumation of the granulitized eclogite terrane in Bhutan are that it is bound at its roof by a normal-sense boundary (the STD,

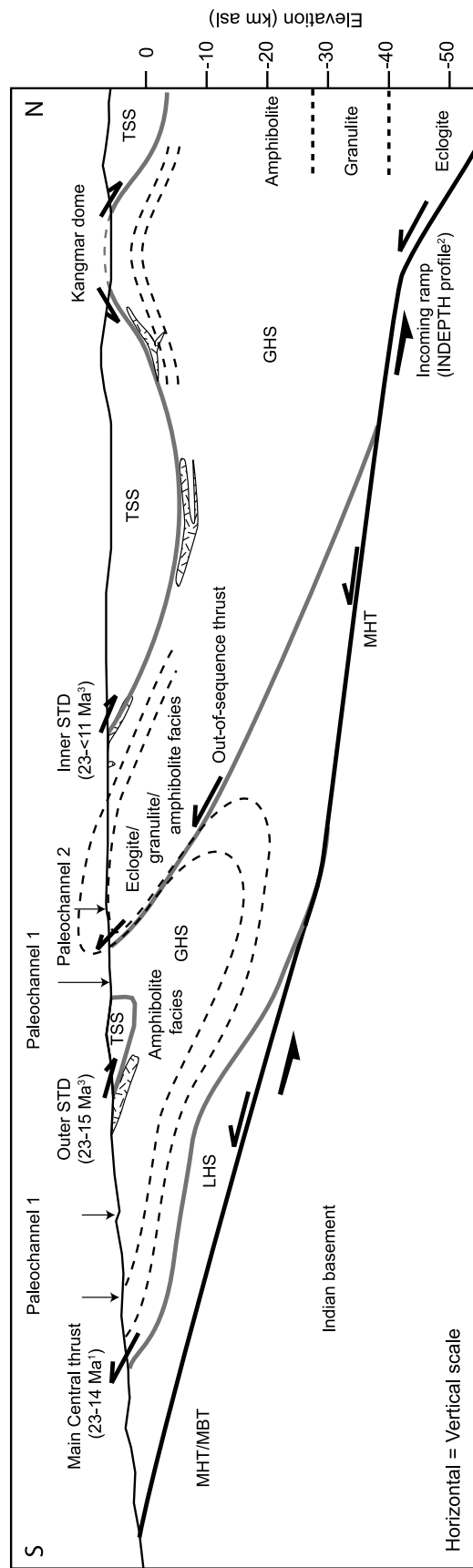


Figure 10. Interpretive N-S cross section through NW Bhutan. The dashed lines are marker lines. MBT, Main Boundary Thrust; MCT, Main Central Thrust; MHT, Main Himalayan Thrust; STD, South Tibetan Detachment; GHS, Greater Himalayan Sequence; LHS, Lesser Himalayan Sequence; TSS, Tethyan Sedimentary Sequence. Numerals are as follows: 1, Daniel et al. [2003]; 2, Hauck et al. [1998]; 3, Kellett et al. [2009].

active until at least 11 Ma [Kellett *et al.*, 2009]), at its base by a contemporaneously operating thrust sense boundary (the “Laya Thrust,” which, if the westward extension of the Kakhtang Thrust, operated after circa 15 Ma [Daniel *et al.*, 2003]), that it reached higher metamorphic grade than the terrane directly underlying it (eclogite and granulite rather than amphibolite), and that peak T metamorphism and anatexis occurred later (15–13 Ma) than in the underlying terrane (20–17 Ma). The granulite terrane in Bhutan may therefore be considered either as a coherent slab in which exhumation occurred contemporaneously across its breadth (the “wedge” model [Vannay *et al.*, 2004]) or as the solidified remains of weak rock that once flowed between more rigid boundaries as it exhumed (the “channel flow” model [Beaumont *et al.*, 2001; Grujic *et al.*, 2002; Beaumont *et al.*, 2004; Godin *et al.*, 2006; Jamieson *et al.*, 2006]). There has been much debate about which of these models may provide a better explanation of Himalayan evolution [Harrison, 2006]; however the best fit model to some extent depends on the time frame under investigation [e.g., Harris, 2007; Beaumont and Jamieson, 2010]. The ubiquity of migmatitic textures across the unit attests to partial melting and consequent crustal weakening, even at <10% melt by volume [Rosenberg and Handy, 2005], during the granulite to amphibolite grade stage of the metamorphic history. This favors the channel flow mechanics for exhumation of this terrane.

[39] Channelized flow of relatively weak material in a near-horizontal crustal channel (as opposed to flow in a steep subduction channel) may be driven toward the surface by a combination of pressure gradient (here the difference between the thickened crust of the Tibetan Plateau and the foreland) and focused erosion (here at the Himalayan front). Among the array of numerical geodynamic channel flow models with relevance to Himalayan tectonics, Model HT111 [Jamieson *et al.*, 2006] predicts the behavior of melt-weakened middle crust below upper crust containing a weak layer. This model shows features which are similar to those described from Bhutan, and may help provide insight into the driving forces behind the exhumation of the eastern Himalayan high-grade rocks. The embedded upper crustal weak layer facilitates the destabilization, detachment and foreland-directed flow of the upper crust, allowing the orogen to form a southward propagating fold-thrust-belt in the foreland. This causes a rapid advance of the orogenic front, which combined with the rapid outward flow of the hot weak crustal channel, does not allow the incoming crust time to completely thermally reequilibrate and hence forms a relatively cool, strong crustal ramp. Hot, weak, channel material in the interior of the orogen is forced over this ramp, destabilizing the weak overlying upper crust, which if it breaks, may form structures analogous to the north Himalayan gneiss domes [Beaumont *et al.*, 2006; Jamieson *et al.*, 2006]. In Model HT111, domes are extruded beneath the upper crust and toward the orogenic front, and are emplaced over previously exhumed channel material along an out-of-sequence thrust which duplicates the high-grade section. Model P-T-t paths from the extruded dome display isothermal decompression from >1.3 GPa to <0.4 GPa between 18 Ma and 6 Ma model time [Jamieson *et al.*, 2006,

Figure 9], and record higher PT conditions than previously extruded material.

[40] Although Model HT 111 was not specifically designed to reproduce particular cross sections in the eastern Himalaya, data from NW Bhutan are consistent with, and may be compared to, the predictions of this model. First, lower-grade metamorphic rocks yielding older ages (the granulite-absent, upper amphibolite-facies terrane) are overlain by higher-grade rocks yielding younger ages (the granulite ± eclogite-bearing terrane), suggesting the presence of an out-of-sequence thrust (Figures 1b, 1c and 10). The granulite terrane may therefore represent (part of) an exhumed dome, as recently proposed by Kellett *et al.* [2010]. Modeled peak P-T conditions, predicting a broad high-grade region with >800°C and 0.8–1.2 GPa, are consistent with data from NW Bhutan [Jamieson *et al.*, 2006]. Second, INDEPTH seismic reflections have been interpreted to show a ~35 km high ramp in the Main Himalayan Thrust at approximately the present latitude of the Kangmar Dome, ~40 km north of the Bhutan-Tibet border [Hauck *et al.*, 1998]. We suggest that a similar structure may have been responsible for exhumation of granulite-facies and relict HP rocks above the Kakhtang Thrust in Bhutan at circa 15 Ma.

[41] The comparison between numerical model predictions and data suggests that exhumation of granulite-facies material from lower crustal depths over a crustal ramp is physically plausible (Figure 10); in concept this idea has previously been explored [e.g., Guillot *et al.*, 2008]. Rapid exhumation of deeply buried rocks may therefore be driven by tectonics as well as by buoyancy. Similar “plunger” mechanisms have previously been suggested for the exhumation of HP rocks in a subduction channel [Warren *et al.*, 2008]. Exhumation rates in the plunger models are in the order of 0.5–1.7 cm a⁻¹ for initial exhumation from mantle depths to midcrustal levels; these are comparable to buoyancy-driven models with exhumation rates of 1.2–1.5 cm a⁻¹ [Warren *et al.*, 2008]. Model exhumation rates depend heavily on material viscosity and the viscosity difference between the plunger and the expelled material. Although absolute values are different, the pattern of faster exhumation for buoyancy-driven exhumation compared with slower exhumation for tectonically driven exhumation is matched by data from the Himalayan eclogites: faster rates of 0.3–0.8 cm a⁻¹ for the Kaghan terrane [Parrish *et al.*, 2006] and slower rates of ~0.3 cm a⁻¹ for the Bhutan terrane (assuming a crustal density of 2800 kg m⁻³ and granulite-facies pressures of 1.0 GPa at 14 Ma). These back-of-the-envelope calculations are by necessity averages, and it is plausible that initial exhumation over the ramp could have been faster, followed by later, slower, surface-denudation-controlled exhumation.

[42] Although similar PTt data have been reported for the Ama Drime/Arun eclogites, their structural position and hence the tectonic process driving their final exhumation to the surface, appears to be different [Cottle *et al.*, 2009a; Corrie *et al.*, 2010; Kali *et al.*, 2010]. The Ama Drime range is bounded by north-south striking faults which appear to have accommodated significant orogen-parallel E-W extension since 13 Ma [Jessup *et al.*, 2008; Cottle *et al.*, 2009a].

These workers suggest that extension on these structures coupled with focused denudation in the Arun River gorge accommodated the exhumation of the high-grade rocks in the footwall. Such large-scale orogen-parallel extension is not seen in Bhutan, whereas no south directed out-of-sequence thrusting has been observed in the Ama Drime Massif. Therefore although comparable rocks appear to have originated from similar crustal levels, their exhumation, or at least the later stages of their exhumation, appears to have been driven by fundamentally different processes.

6. Conclusions

[43] U-Pb geochronology suggests that monazites in the leucosome of granulite-grade pelitic garnet-orthopyroxene-biotite-plagioclase migmatitic gneisses exposed in Bhutan, E Himalaya, crystallized at 13.9 ± 0.3 Ma. Evidence from associated mafic rocks suggests that granulite-facies conditions were reached after an earlier HP eclogite-facies event, the conditions and timing of which remain cryptic. Monazite associated with sillimanite-grade metamorphism in granulite-hosting garnet-sillimanite-biotite migmatitic gneisses yields rim ages between 15.4 ± 0.8 Ma and 13.4 ± 0.5 Ma. These rocks structurally overlie older 21–17 Ma garnet-sillimanite-biotite migmatitic gneisses which do not record evidence for granulite-facies metamorphism. The geochronological, petrological and structural data suggest that an out-of-sequence thrust separates the two packages, although this hypothesis requires more detailed mapping.

[44] The eastern Himalayan granulitized eclogites do not provide evidence for diachronous collision across the orogen.

References

- Beaumont, C., and R. Jamieson (2010), Himalayan-Tibetan orogeny: Channel flow versus (critical) wedge models, a false dichotomy, in *Proceedings for the 25th Himalaya-Karakoram-Tibet Workshop*, edited by M. L. Leech, S. L. Klempner, and W. D. Mooney, *U.S. Geol. Surv. Open File Rep., 2010-1099*, 2 pp. (Available at <http://pubs.usgs.gov/2010/1099/beaumont/>.)
- Beaumont, C., R. A. Jamieson, M. H. Nguyen, and B. Lee (2001), Himalayan tectonics explained by extrusion of a low-viscosity crustal channel coupled to focused surface denudation, *Nature*, **414**, 738–742, doi:10.1038/414738a.
- Beaumont, C., R. A. Jamieson, M. H. Nguyen, and S. Medvedev (2004), Crustal channel flows: I. Numerical models with applications to the tectonics of the Himalayan-Tibetan orogen, *J. Geophys. Res.*, **109**, B06406, doi:10.1029/2003JB002809.
- Beaumont, C., M. Nguyen, R. A. Jamieson, and S. Ellis (2006), Crustal flow modes in large hot orogens, in *Channel Flows, Ductile Extrusion and Exhumation in Continental Collision Zones*, edited by R. D. Law, M. P. Searle, and L. Godin, *Geol. Soc. Spec. Publ.*, **268**, 91–145.
- Beaumont, C., R. A. Jamieson, J. P. Butler, and C. J. Warren (2009), Crustal structure: A key constraint on the mechanism of ultra-high-pressure rock exhumation, *Earth Planet. Sci. Lett.*, **287**, 116–129, doi:10.1016/j.epsl.2009.08.001.
- Bhargava, O. N. (1995), *The Bhutan Himalaya: A Geological Account, Spec. Publ. Ser. Geol. Surv. India*, **39**, 245 pp.
- Carosi, R., C. Montomoli, D. Rubatto, and D. Visona (2006), Normal-sense shear zones in the core of the Higher Himalayan crystallines (Bhutan Himalaya): Evidence for extrusion?, *Geol. Soc. Spec. Publ.*, **268**, 425–444, doi:10.1144/GSL.SP.2006.268.01.20.
- Carrington, D. P., and S. L. Harley (1995), Partial melting and phase relations in high-grade metapelites: An experimental petrogenetic grid in the KFMASH system, *Contrib. Mineral. Petrol.*, **120**, 270–291, doi:10.1007/BF00306508.
- Chakungal, J. (2006), Geochemistry and metamorphism of metabasites, and spatial variation of P-T paths across the Bhutan Himalaya: Implications for the exhumation of the Greater Himalayan Sequence, Ph.D. thesis, 1–169 pp., Dalhousie Univ., Dalhousie, N. S., Canada.
- Chakungal, J., J. Dostal, D. Grujic, S. Duchêne, and K. S. Ghally (2010), Provenance of the Greater Himalayan Sequence: Evidence from mafic granulites and amphibolites in NW Bhutan, *Tectonophysics*, **480**, 198–212, doi:10.1016/j.tecto.2009.10.014.
- Corrie, S. L., M. J. Kohn, and J. D. Vervoort (2010), Young eclogite from the Greater Himalayan Sequence, Arun Valley, eastern Nepal: P-T-t path and tectonic implications, *Earth Planet. Sci. Lett.*, **289**, 406–416, doi:10.1016/j.epsl.2009.11.029.
- Cottle, J. M., M. J. Jessup, D. L. Newell, M. S. A. Horstwood, S. R. Noble, R. R. Parrish, D. J. Waters, and M. P. Searle (2009a), Geochronology of granulitized eclogite from the Ama Drime Massif: Implications for the tectonic evolution of the South Tibetan Himalaya, *Tectonics*, **28**, TC1002, doi:10.1029/2008TC002256.
- Cottle, J. M., M. S. A. Horstwood, and R. R. Parrish (2009b), A new approach to single shot laser ablation analysis and its application to in situ Pb/U geochronology, *J. Anal. At. Spectrom.*, **24**, 1355–1363, doi:10.1039/b821899d.
- Cottle, J. M., M. P. Searle, M. S. A. Horstwood, and D. J. Waters (2009c), Timing of midcrustal metamorphism, melting, and deformation in the Mount Everest region of southern Tibet revealed by U-Th-Pb geochronology, *J. Geol.*, **117**, 643–664, doi:10.1086/605994.
- Daniel, C. G., L. S. Hollister, R. R. Parrish, and D. Grujic (2003), Exhumation of the Main Central Thrust from lower crustal depths, eastern Bhutan Himalaya, *J. Metamorph. Geol.*, **21**, 317–334, doi:10.1046/j.1525-1314.2003.00445.x.
- Davidson, C., D. E. Grujic, L. S. Hollister, and S. M. Schmid (1997), Metamorphic reactions related to decompression and synkinematic intrusion of leucogranite, High Himalayan crystallines, Bhutan pa, *J. Metamorph. Geol.*, **15**, 593–612, doi:10.1111/j.1525-1314.1997.00044.x.
- de Sigoyer, J., V. Chavagnac, J. Blichert-Toft, I. M. Villa, B. Luais, S. Guillot, M. Cosca, and G. Mascle (2000), Dating the Indian continental subduction and collisional thickening in the northwest Himalaya: Multichronology of the Tso Morari eclogites, *Geology*, **28**, 487–490, doi:10.1130/0091-7613(2000)28<487:DTICSA>2.0.CO;2.
- Edwards, M. A., and T. M. Harrison (1997), When did the roof collapse? Late Miocene north-south extension in the high Himalaya revealed by Th-Pb monazite dating of the Khula Kangri granite, *Geology*, **25**, 543–546, doi:10.1130/0091-7613(1997)025<543:WDTRCL>2.3.CO;2.
- England, P., and P. Molnar (1990), Surface uplift, uplift of rocks, and exhumation of rocks, *Geology*, **18**, 1173–1177, doi:10.1130/0091-7613(1990)018<1173:SUUORA>2.3.CO;2.
- Epard, J.-L., and A. Steck (2008), Structural development of the Tso Morari ultra-high pressure nappe of the Ladakh Himalaya, *Tectonophysics*, **451**, 242–264, doi:10.1016/j.tecto.2007.11.050.
- Ernst, W. G., S. Maruyama, and S. Wallis (1997), Buoyancy-driven, rapid exhumation of ultrahigh-pressure metamorphosed continental crust, *Proc.*

Instead they suggest a distinct episode of eclogite formation tectonically unrelated to the early subduction-related, buoyantly exhumed eclogites in the western Himalaya. As there is no evidence for the presence of a subduction zone in the eastern Himalaya in the mid-Miocene, buoyancy-related exhumation in a subduction channel is not considered a viable mechanism for the exhumation of these high-grade rocks. Instead, available seismic data combined with insight from previously published numerical models suggest that granulite ± eclogite facies rocks may have been exhumed over older, colder, previously exhumed middle crustal material during penetration of a strong Indian crustal ramp into the thickened weak Himalayan orogenic crust. Synconvergent exhumation of lower crustal level eclogite-facies material may therefore be achieved by tectonic (plunger) forcing rather than by buoyancy in the absence of a subduction system.

[45] **Acknowledgments.** C.J.W. acknowledges current postdoctoral funding from the Natural Environment Research Council (NE/E0114038/1) and a previous Killam Postdoctoral Fellowship held at Dalhousie University. D.G. and R.A.J. acknowledge funding from NSERC Discovery grants. Some of the BH samples were collected and/or initially characterized by Joyia Chakungal and David Moynihan. Patricia Stoffyn and Andy Tindle are gratefully acknowledged for help in the Dalhousie and Open University microprobe laboratories. Matt Horstwood, Vanessa Pashley, and Nick Lloyd are gratefully acknowledged for analytical help at NIGL, and NIGFSC grant IP/1054/0508 covered analytical costs. Dick Brown is thanked for allowing us access to the RLB samples. Fantastic logistical support from numerous guides, drivers, cooks, and camp crew in Bhutan eased our way during fieldwork. We thank two anonymous reviewers for constructive criticism and Onno Oncken for editorial handling.

- Natl. Acad. Sci. U. S. A.*, 94, 9532–9537, doi:10.1073/pnas.94.18.9532.
- Foster, G., H. D. Gibson, R. Parrish, M. Horstwood, J. Fraser, and A. Tindle (2002), Textural, chemical and isotopic insights into the nature and behaviour of metamorphic monazite, *Chem. Geol.*, 191, 183–207, doi:10.1016/S0009-2541(02)00156-0.
- Ganguly, J., S. Dasgupta, W. Cheng, and S. Neogi (2000), Exhumation history of a section of the Sikkim Himalayas, India: Records in the metamorphic mineral equilibria and compositional zoning of garnet, *Earth Planet. Sci. Lett.*, 183, 471–486, doi:10.1016/S0012-821X(00)00280-6.
- Gansser, A. (1983), *Geology of the Bhutan Himalaya*, 181 pp., Birkhäuser, Basel, Switzerland.
- Godin, L., D. Grujic, R. D. Law, and M. P. Searle (2006), Channel flow, ductile extrusion and exhumation in continental collision zones: An introduction, *Geol. Soc. Spec. Publ.*, 268, 1–23, doi:10.1144/GSL.SP.2006.268.01.01.
- Goscombe, B., D. Gray, and M. Hand (2006), Crustal architecture of the Himalayan metamorphic front in eastern Nepal, *Gondwana Res.*, 10, 232–255, doi:10.1016/j.gr.2006.05.003.
- Groppi, C., B. Lombardo, F. Rolfo, and P. Pertusati (2007), Clockwise exhumation path of granulitized eclogites from the Ama Drime range (Eastern Himalayas), *J. Metamorph. Geol.*, 25, 51–75, doi:10.1111/j.1525-1314.2006.00678.x.
- Grujic, D., L. S. Hollister, and R. R. Parrish (2002), Himalayan metamorphic sequence as an orogenic channel: Insight from Bhutan, *Earth Planet. Sci. Lett.*, 198, 177–191, doi:10.1016/S0012-821X(02)00482-X.
- Guillot, S., M. Cosca, P. Allemand, and P. Le Fort (1999), Contrasting metamorphic and geochronological evolution along the Himalayan belt, in *Himalaya and Tibet: Mountain Roots to Mountain Tops*, edited by A. Macfarlane, R. B. Sorkhabi, and J. Quade, *Spec. Pap. Geol. Soc. Am.*, 328, 117–128.
- Guillot, S., G. Mahéo, J. de Sigoyer, K. H. Hattori, and A. Pécher (2008), Tethyan and Indian subduction viewed from the Himalayan high- to ultrahigh-pressure metamorphic rocks, *Tectonophysics*, 451, 225–241, doi:10.1016/j.tecto.2007.11.059.
- Harris, N. (2007), Channel flow and the Himalayan-Tibetan orogen: A critical review, *J. Geol. Soc.*, 164, 511–523, doi:10.1144/0016-76492006-133.
- Harrison, T. M. (2006), Did the Himalayan crystallines extrude partially molten from beneath the Tibetan Plateau?, *Geol. Soc. Spec. Publ.*, 268, 237–254.
- Hauck, M. L., K. D. Nelson, L. D. Brown, W. Zhao, and A. R. Ross (1998), Crustal structure of the Himalayan orogen at ~90° east longitude from Project INDEPTH deep reflection profiles, *Tectonics*, 17, 481–500, doi:10.1029/98TC01314.
- Hodges, K. V. (2000), Tectonics of the Himalaya and southern Tibet from two perspectives, *Geol. Soc. Am. Bull.*, 112, 324–350, doi:10.1130/0016-7606(2000)112<324:TOHTAS>2.0.CO;2.
- Hollister, L. S., and D. Grujic (2006), Pulsed channel flow in Bhutan, *Geol. Soc. Spec. Publ.*, 268, 415–423, doi:10.1144/GSL.SP.2006.268.01.19.
- Horstwood, M. S. A., G. L. Foster, R. R. Parrish, S. R. Noble, and G. M. Nowell (2003), Common-Pb corrected in situ U-Pb accessory mineral geochronology by LA-MC-ICP-MS, *J. Anal. At. Spectrom.*, 18, 837–846, doi:10.1039/b304365g.
- Jamieson, R. A., C. Beaumont, M. H. Nguyen, and D. Grujic (2006), Provenance of the Greater Himalayan Sequence and associated rocks: Predictions of channel flow models, *Geol. Soc. Spec. Publ.*, 268, 165–182, doi:10.1144/GSL.SP.2006.268.01.07.
- Jessup, M. J., D. L. Newell, J. M. Cottle, A. L. Berger, and J. A. Spotila (2008), Orogen-parallel extension and exhumation enhanced by denudation in the trans-Himalayan Arun River gorge, Ama Drime Massif, Tibet-Nepal, *Geology*, 36, 587–590, doi:10.1130/G24722A.1.
- Kali, E., P. H. Leloup, N. Arnaud, G. Mahéo, D. Liu, E. Boutonnet, J. Van der Woerd, X. Liu, J. Liu, Zheng, and H. Li (2010), Exhumation history of the deepest central Himalayan rocks, Ama Drime range: Key pressure-temperature-deformation-time constraints on orogenic models, *Tectonics*, 29, TC2014, doi:10.1029/2009TC002551.
- Kaneko, Y., I. Katayama, H. Yamamoto, K. Misawa, M. Ishikawa, H. U. Rehman, A. B. Kausar, and K. Shiraishi (2003), Timing of Himalayan ultrahigh-pressure metamorphism: Sinking rate and subduction angle of the Indian continental crust beneath Asia, *J. Metamorph. Geol.*, 21, 589–599, doi:10.1046/j.1525-1314.2003.00466.x.
- Kellett, D. A., D. Grujic, and S. Erdmann (2009), Miocene structural reorganization of the South Tibetan detachment, eastern Himalaya: Implications for continental collision, *Lithosphere*, 1, 259–281, doi:10.1130/L56.1.
- Kellett, D. A., D. Grujic, C. J. Warren, J. Cottle, R. A. Jamieson, and T. Tenzin (2010), Metamorphic history of a syn-convergent orogen-parallel detachment: The South Tibetan detachment system, Bhutan Himalaya, *J. Metamorph. Geol.*, 28, 785–808, doi:10.1111/j.1525-1314.2010.00893.x.
- Kelsey, D. E., C. Clark, and M. Hand (2008), Thermo-barometric modelling of zircon and monazite growth in melt-bearing systems: Examples using model metapelitic and metapsammitic granulites, *J. Metamorph. Geol.*, 26, 199–212, doi:10.1111/j.1525-1314.2007.00757.x.
- Kohn, M. J., and M. A. Malloy (2004), Formation of monazite via prograde metamorphic reactions among common silicates: Implications for age determinations, *Geochim. Cosmochim. Acta*, 68, 101–113, doi:10.1016/S0016-7037(03)00258-8.
- Leech, M. L., S. Singh, A. K. Jain, S. L. Klemperer, and R. M. Manickavasagam (2005), The onset of India-Asia continental collision: Early, steep subduction required by the timing of UHP metamorphism in the western Himalaya, *Earth Planet. Sci. Lett.*, 234, 83–97, doi:10.1016/j.epsl.2005.02.038.
- Liu, S., J. Zhang, G. Shu, and Q. Li (2005), Mineral chemistry, P-T-t paths and exhumation processes of mafic granulites in Dinggye, southern Tibet, *Sci. China, Ser. D*, 48, 1870–1881, doi:10.1360/04yd0161.
- Liu, Y., W. Siebel, H. J. Massonne, and X. C. Xiao (2007), Geochronological and petrological constraints for tectonic evolution of the central Greater Himalayan Sequence in the Kharta area, southern Tibet, *J. Geol.*, 115, 215–230, doi:10.1086/510806.
- Lombardo, B., and F. Rolfo (2000), Two contrasting eclogite types in the Himalayas: Implications for the Himalayan orogeny, *J. Geod.*, 30, 37–60, doi:10.1016/S0264-3707(99)00026-5.
- Lombardo, B., P. Pertusati, F. Rolfo, and D. Visonà (1998), First report of eclogites from the Eastern Himalaya: Implications for the Himalayan orogeny, *Mem. Sci. Geol.*, 50, 67–68.
- Ludwig, K. K. (2001), *Isoplot/Ex Version 2.49: A Geochronological Toolkit for Microsoft Excel*, Berkeley Geochronol. Cent., Berkeley, Calif.
- Möller, C. (1998), Decompressed eclogites in the Sveconorwegian (-Grenvillian) orogen of SW Sweden: Petrology and tectonic implications, *J. Metamorph. Geol.*, 16, 641–656, doi:10.1111/j.1525-1314.1998.00160.x.
- Molnar, P., and J. M. Stock (2009), Slowing of India's convergence with Eurasia since 20 Ma and its implications for Tibetan mantle dynamics, *Tectonics*, 28, TC3001, doi:10.1029/2008TC002271.
- Nelson, K. D., et al. (1996), Partially molten middle crust beneath southern Tibet: Synthesis of Project INDEPTH results, *Science*, 274, 1684–1688, doi:10.1126/science.274.5293.1684.
- Neogi, S., S. Dasgupta, and M. Fukuoka (1998), High P-T polymetamorphism, dehydration melting, and generation of migmatites and granites in the Higher Himalayan crystalline complex, Sikkim, India, *J. Petrol.*, 39, 61–99, doi:10.1093/petrology/39.1.61.
- O'Brien, P. J. (1990), Eclogite formation and distribution in the European Variscides, in *Eclogite Facies Rocks*, edited by D. A. Carswell, pp. 204–224, Chapman and Hall, Glasgow, U. K.
- O'Brien, P. J., and J. Rötzler (2003), High-pressure granulites: Formation, recovery of peak conditions and implications for tectonics, *J. Metamorph. Geol.*, 21, 3–20, doi:10.1046/j.1525-1314.2003.00420.x.
- Paquette, J. L., A. Nédélec, B. Moine, and M. Rakotondrazafy (1994), U-Pb, single zircon Pb-evaporation, and Sm-Nd isotopic study of a granulite domain in SE Madagascar, *J. Geol.*, 102, 523–538, doi:10.1086/629696.
- Parrish, R. R. (1990), U-Pb dating of monazite and its application to geological problems, *Can. J. Earth Sci.*, 27, 1431–1450.
- Parrish, R. R., S. J. Gough, M. P. Searle, and D. J. Waters (2006), Plate velocity exhumation of ultrahigh-pressure eclogites in the Pakistan Himalaya, *Geology*, 34, 989–992, doi:10.1130/G22796A.1.
- Patino Douce, A. E., and N. Harris (1998), Experimental constraints on Himalayan anatexis, *J. Petrol.*, 39, 689–710, doi:10.1093/petrology/39.4.689.
- Platt, J. P. (1993), Exhumation of high-pressure rocks: A review of concepts and processes, *Terra Nova*, 5, 119–133, doi:10.1111/j.1365-3121.1993.tb00237.x.
- Ring, U., M. T. Brandon, S. D. Willett, and G. S. Lister (1999), Exhumation processes: Normal faulting, ductile flow and erosion, *Geol. Soc. Spec. Publ.*, 154, 1–27, doi:10.1144/GSL.SP.1999.154.01.01.
- Rolfo, F., R. Carosi, C. Montomoli, and D. Visonà (2008), Discovery of granulitized eclogite in North Sikkim expands the Eastern Himalaya high-pressure province, *Himalayan J. Sci.*, 5, 126–127.
- Rosenberg, C. L., and M. R. Handy (2005), Experimental deformation of partially melted granite revisited: Implications for the continental crust, *J. Metamorph. Geol.*, 23, 19–28, doi:10.1111/j.1525-1314.2005.00555.x.
- Rowley, D. B. (1996), Age of initiation of collision between India and Asia: A review of stratigraphic data, *Earth Planet. Sci. Lett.*, 145, 1–13, doi:10.1016/S0012-821X(96)00201-4.
- Rowley, D. B. (1998), Minimum age of initiation of collision between India and Asia north of Everest based on the subsidence history of the Zephure Mountain section, *J. Geol.*, 106, 220–235, doi:10.1086/516018.
- Schärer, U. (1984), The effect of initial ²³⁰Th disequilibrium on young U-Pb ages: The Makalu case, Himalaya, *Earth Planet. Sci. Lett.*, 67, 191–204, doi:10.1016/0012-821X(84)90114-6.
- Searle, M. P. (1999), Extensional and compressional faults in the Everest Lhotse massif, Khumbu Himalaya, Nepal, *J. Geol. Soc.*, 156, 227–240, doi:10.1144/gsjgs.156.2.0227.
- Spear, F. L., M. J. Kohn, and J. T. Cheney (1999), P-T paths from anatetic pelites, *Contrib. Mineral. Petrol.*, 134, 17–32, doi:10.1007/s004100050466.
- Swapp, S. M., and L. S. Hollister (1991), Inverted metamorphism within the Tibetan slab of Bhutan: Evidence for a tectonically transported heat source, *Can. Mineral.*, 29, 1019–1041.
- Vannay, J.-C., B. Grasemann, M. Rahn, W. Frank, A. Carter, V. Baudraz, and M. Cosca (2004), Miocene to Holocene exhumation of metamorphic crustal wedges in the NW Himalaya: Evidence for tectonic extrusion coupled to fluvial erosion, *Tectonics*, 23, TC1014, doi:10.1029/2002TC001429.
- Warren, C. J., C. Beaumont, and R. A. Jamieson (2008), Modeling tectonic styles and ultra-high pressure (UHP) rock exhumation in the transition from oceanic subduction to continental collision, *Earth Planet. Sci. Lett.*, 267, 129–145, doi:10.1016/j.epsl.2007.11.025.
- Whitney, D. L., and B. W. Evans (2010), Abbreviations for names of rock-forming minerals, *Am. Mineral.*, 95, 185–187, doi:10.2138/am.2010.3371.
- Wu, C., K. D. Nelson, G. Wortman, S. D. Samson, Y. Yue, J. Li, W. S. F. Kidd, and M. A. Edwards (1998), Yadong cross structure and South Tibetan Detachment in the east central Himalaya (89°–90°E), *Tectonics*, 17, 28–45, doi:10.1029/97TC03386.
- Zhao, G., P. A. Cawood, S. A. Wilde, and L. Lu (2000), High-pressure granulites (retrograded eclogites)

- from the Hengshan Complex, North China Craton: Petrology and tectonic implications, *J. Petrol.*, 42, 1141–1170, doi:10.1093/petrology/42.6.1141.
- Zhu, B., W. Kidd, D. Rowley, B. Currie, and N. Shafique (2005), Age of initiation of the India-Asia collision in the east-central Himalaya, *J. Geol.*, 113, 265–285, doi:10.1086/428805.

J. Cottle and D. A. Kellett, Department of Earth Science, University of California, Santa Barbara, CA 93106-9630, USA.

K. S. Ghalley, Geological Survey of Bhutan, Department of Geology and Mines, Ministry of Economic Affairs, Post Box 173, Thimphu, Bhutan.

D. Grujic and R. A. Jamieson, Department of Earth Sciences, Dalhousie University, Halifax, NS B3H 4J1, Canada.

C. J. Warren, Department of Earth and Environmental Sciences, CEPSAR, Open University, Walton Hall, Milton Keynes MK7 6AA, UK. (c.warren@open.ac.uk)